6-22-2021 2:00 PM

Developing sodium MRI for longitudinal assessment of chemotherapy of glioma in a rat model of cancer

Xin Yue Wang, *The University of Western Ontario*

Supervisor: Scholl, Timothy J., *Robarts Research Institute*
A thesis submitted in partial fulfillment of the requirements for the Master of Science degree in Medical Biophysics

Recommended Citation

Wang, Xin Yue, "Developing sodium MRI for longitudinal assessment of chemotherapy of glioma in a rat model of cancer" (2021). *Electronic Thesis and Dissertation Repository*. 8077.
https://ir.lib.uwo.ca/etd/8077

Abstract

Glioblastoma (GBM) is an aggressive cancer which presents significant challenges for disease management and treatment. Tissue sodium concentration (TSC) is a sensitive indicator of disease and changes in TSC can be used as a potential biomarker for treatment response. A longitudinal orthotopic C6 GBM model was used to study changes in TSC due to cancer. Animals were imaged with contrast enhanced T_1-weighted, T_2-weighted and sodium MRI and were either un-treated or received temozolomide (TMZ) treatment. Accurate assessment of TSC was possible for tumour volumes greater than 150mm^3 using 3mm isotropic imaging voxels. TSC increased with tumour growth for all animals. However, no differences in TSC were observed between treated and non-treated animals. This study demonstrates the feasibility of preclinical sodium MRI at 3T and highlights future potential challenges to overcome for this modality.

Keywords

Glioblastoma multiform, magnetic resonance imaging, multi-nuclear magnetic resonance imaging, C6 rat model

Summary for Lay Audience

Glioblastoma (GBM) is an aggressive brain cancer which presents significant challenges for disease management and treatment. Tissue sodium concentration (TSC) is a sensitive indicator of disease and observing changes in TSC can provide additional information about tumour biology. Magnetic resonance imaging (MRI) is a powerful non-invasive imaging modality which uses the physics underlying magnetism to obtain images of the body. MRI can capture the differences between soft tissues and provide detailed structural and morphological information about internal areas of the body. Standard MRI relies on the hydrogen atoms found in the body – particularly in the water to capture these images. Sodium MRI applies the same principles used in standard MRI but instead on sodium atoms found throughout the body, providing TSC information. In this study, C6 rats were implanted with GBM brain tumours and imaged longitudinally using standard MRI techniques and sodium MRI. Animals were either untreated, or received treatment using temozolomide (TMZ) – the chemotherapy drug used to treat GBM. Accurate assessment of TSC was possible for tumour volumes greater than 150mm^3 using 3mm isotropic imaging voxels. TSC increased with tumour growth for all animals. However, there were no differences in TSC changes between treated and non-treated animals. Ultimately TSC at endpoint was lower for treated animals, however this difference was not significant. This study demonstrates the feasibility of preclinical sodium MRI at 3T and highlights future potential challenges to overcome for this modality.

Acknowledgements

I would like to thank the following individuals who supported my research and my education as a trainee. I would like to thank my supervisor Dr. Timothy J. Scholl for his unending support over the course of this project, especially through the global COVID-19 pandemic. In addition, I would like to thank my advisory committee members Drs. Lisa Hoffman, Jonathan Theissen, and Matthew Hebb who were indispensable for their support and advice throughout my thesis.

Additional special thanks goes to Dr. Francisco M. Martinez-Santiesteban for accompanying me through my imaging and providing support for many technical aspects of this project. This gratitude is also extended to Dr. Alireza Akbari for his major role guiding me through the nuances of sodium imaging.

I would like to thank my fellow lab mates in the Cellular and Molecular Imaging Group, especially for teaching me many new skills, supporting, and uplifting me, and answering my many questions.

Special thanks also goes out to Andrew Olin and Andrew Dewyert who were essential to teaching me important skills without which this research would not have be possible. Additional thanks goes to Brian Dalrymple and Frank Van Sas for the fabrication of the animal bed used for the imaging.

Lastly, I would like to acknowledge the funding from NSERC and OICR without whom this research would not have been possible.

Table of Contents

List of Tables

List of Figures

List of Appendices

List of Abbreviations

α	Flip angle
γ	Gyromagnetic ratio
ω_0	Larmor frequency
^{1}H	Hydrogen ion (proton)
^{19}F	Fluorine
^{23}Na	Sodium
2D	Two-dimensional
3D	Three-dimensional
3DPR	Three-dimensional projection reconstruction
ATP	Adenosine 5' triphosphate
$\overrightarrow{B_0}$	External magnetic field
$\overrightarrow{B_1}$	Oscillating magnetic field
BBB	Blood brain barrier
C	Capacitance
CE	Contrast enhancement
CNS	Central nervous system
CO_2	Carbon dioxide
CR	Complete response
CSF	Cerebral spinal fluid
CT	Computed tomography
DA3DPR	Density-adapted 3-dimensional projection reconstruction
DMEM	Dulbecco's modified eagle medium
DTPA	Diethylenetriamine pentaacetate
ETL	Echo train length
FBS	Fetal bovine serum
FLAIR	Fluid attenuated inversion recovery
FOV	Field of view
FSE	Fast-spin echo
GBM	Glioblastoma multiforme
Gd	Gadolinium
Gy	Gray
Hz	Hertz

mg	Milligram
MHz	Megahertz
mL	Milliliter
mm	Millimeter
mM	Millimoles
MPI	Magnetic particle imaging
MRI	Magnetic resonance imaging
ms	Millisecond
mT	Millitesla
NaCl	Sodium chloride
NEX	Number of excitations (averages)
NHE	Sodium proton antiporter
NHE1	Sodium proton antiporter isoform 1
OCT	Optimal cutting temperature
OD	Outer diameter
PBS	Phosphate buffer solution
PD	Progressive disease
PET	Positron emission tomography
PFA	Paraformaldehyde
pH	Power of hydrogen
PR	Partial response
RANO	Response Assessment in Neuro-Oncology
RF	Radiofrequency
s	Seconds
SD	Stable disease
SNR	Signal-to-noise ratio
T	Tesla
T_1	Spin-lattice relaxation time (longitudinal)
T_2	Spin-spin relaxation time (transverse)
T_2*	Effective spin-spin relaxation rate
T_{aq}	Time of acquisition
TE	Time-to-echo
TG	Transmit gain
Tm-DOTP^{5-}	thulium-1,4,7,10-tetraazacyclododecane 1,4,7,10-tetrakis(methylene phosphonate)

TMZ	Temozolomide
TPI	Twisted projection imaging
TR	Time-to-repetition
TSC	Tissue sodium concentration
US	Ultrasound
UTE	Ultrashort echo time
WHO	World Health Organization

Chapter 1

1 General Introduction

1.1 Glioma

Out of all tumours arising in the brain and central nervous system (CNS), gliomas are the most common [1]. In Canada, brain and CNS cancers are predicted to account for 7.1% of all diagnosed cancers for 2020 [2]. Glioma is a general term used to describe tumours arising from glial cells and their precursors and include a variety of subtypes and grades [3]. Between 2009 and 2013 in Canada, tumours arising from these tissues accounted for over 80% of all diagnosed CNS tumours [4]. The World Health Organization (WHO) has released new classification criteria for gliomas, reclassifying them as an astrocytoma based on shared genetic markers. In this grading scheme, grades I and II are considered low-grade tumours, while grades III and IV are considered high grade. Current classification integrates both phenotypic and genotypic characteristics. In general, grade I glioma is the least malignant and can be treated through surgical resection. Grade II glioma is more infiltrative and more likely to recur and progress to higher grades. Grade III and IV gliomas are highly infiltrative and aggressive, and associated with poor prognosis and poor patient outcomes [5]. The following sections will expand on high grade gliomas and the challenges associated with their treatment.

1.1.1 Glioblastoma multiforme

Glioblastoma (GBM) are grade IV gliomas, the most aggressive and infiltrative. Cells from the main GBM tumour will migrate away from the main mass through the brain parenchyma. This results in individual tumour cells diffusing through the brain tissue, over long distances, and potentially into vital regions of the brain. Since these diffuse cells can extend beyond lesions visible by imaging, it becomes more difficult to have a full grasp on the state of the disease. Furthermore, the location of GBM within the brain is often variable and can occur in areas difficult to treat, further compounding aggressiveness of this disease [6]. Additionally, GBM are also the most common malignant primary brain tumours, accounting for 45.6% of all gliomas and 15.4% of all primary brain tumours [7]. The Brain Tumour Registry of Canada reports that 12% to 15% of all intercranial tumours and 50% to 60% of astrocytic tumours are GBM. Median survival for patients is merely 12 to 15 months after diagnosis and only 5% of patients survive to 5 years [8, 9]. GBM is heterogeneous and multiforme on a macro and micro scale. Overall, GBM tumours display regions of hemorrhage and necrosis, as well as regions of pleomorphic nuclei and cells, and microvascular proliferation [6]. GBM can arise as a primary tumour – wherein the cancer arises with no evidence of a precursor, or as a secondary tumour – developing from a lower grade diffuse astrocytoma [10].

1.1.2 Glioblastoma therapy

The clinical standard for GBM treatment is maximal surgical resection, followed by radiotherapy – 60Gy total split over 30 daily fractions of 2Gy each, concurrent with chemotherapy using Temozolomide (TMZ) – administered for 7 days at a daily dose of 75mg/m^2 [11]. However, despite this therapy, overall survival is still poor [8, 9]. Unfortunately, the median time to tumour recurrence is 8 months [5]. This rapid recurrence is likely because treatments cannot eliminate all the tumour cells [8]. Maximal surgical resection is limited by the diffuse nature of the disease; making it difficult to distinguish the cancerous tissue from healthy tissue [8]. It can additionally be limited by the tumour's location in or near vital brain regions, and the rapid growth of the residual cancer stem cells after surgery [5, 6]. Radiotherapy is also limited by the diffuse nature of the disease, as targeted radiotherapy cannot hope to affect individual cells which have spread from the primary tumour. Chemotherapy effectiveness is limited by the blood brain barrier (BBB), restricting drug penetration into brain cells, and the heterogeneity of the cells, resulting in variable effectiveness [5, 8]. Upon GBM recurrence, treatment faces additional challenges. Surgery may not be possible after recurrence. Additionally, chemo- and radiotherapy options are limited at that point. In addition to no standard for second line chemotherapy in GBM treatment, the recurred tumour can acquire a chemo-resistant phenotype [1, 8]. Re-irradiation carries with it a risk of toxicity, as well as brain necrosis or radiation-induced injury [3, 8].

1.2 Sodium and metabolism in biological tissues

Sodium is the most abundant cation in the body and plays a key role in many cellular processes, such as nerve conduction, muscle contraction, and maintaining tissue osmolarity [12, 13]. Changes in sodium distribution within cells and tissues is associated with many pathologies. Sodium concentration (mol/L = M) is maintained at 10-15mM intracellularly and 140mM extracellular in healthy tissue [14]. This section provides background information about the role sodium plays in healthy tissues and the changes that occur in a cancerous phenotype. Changes in pathways regulating sodium form the basis for a heterogeneous sodium distribution that is characteristic of disease.

1.2.1 Tumour metabolism

Sodium concentrations in the intracellular and extracellular space are carefully maintained for regulating proper cell function and volume [12]. The large sodium concentration gradient is maintained by a variety of active transport, voltage, and ligand gated channels. The most prominent transporter involved is the Na^+/K^+-ATPase or the sodium-potassium pump. This plasma membrane protein is expressed in most eukaryotic cells, and functions to maintain the sodium and potassium gradients. By using the energy from hydrolyzing adenosine 5'-triphosphate (ATP), the Na^+/K^+-ATPase transports three sodium ions out of the cell while pumping two potassium ions in, this enables healthy cells to maintain their low intracellular sodium levels [13]. Impairment of Na^+/K^+-ATPase function or cell membrane integrity can lead to an increase of intracellular sodium. Another important transported involved in sodium transport is the Na^+/H^+ antiport (NHE) or the sodium hydrogen antiporter. This membrane protein exchanges one intracellular hydrogen ion for one extracellular sodium. Of the NHEs, isoform I (NHE1) is expressed in most tissues and cells. NHE1 functions to maintain cytosolic pH as well as cellular volume [15]. The significance of sodium exchange acting to maintain intracellular pH is key to the Warburg effect that will be further discussed in section 1.2.2 and 1.2.3.

1.2.2 Sodium ion flux in cells

Healthy cells in a multicellular organism participate in controlled growth by heavily regulating their metabolic pathways. This is required as these cells receive a constant supply of nutrients. Control of metabolic activity prevents aberrant cell proliferation that exceeds nutrient availability. Healthy cells in aerobic conditions produce energy in the form of ATP through the heavily regulated pathway of oxidative phosphorylation in the mitochondria [16]. Lactate is only produced in in anaerobic conditions. Cellular metabolism is altered in cancers, as cell survival and growth are promoted by circumventing oxidative phosphorylation to produce ATP through glycolysis even in aerobic conditions. The Warburg effect describes the tendency of cancer cells to ferment glucose to lactate regardless of oxygenation conditions, resulting in cancer cells undergoing aerobic glycolysis [17]. Aerobic glycolysis is much less efficient than oxidative phosphorylation in the production of ATP, however this process is virtually unregulated and in addition promotes tumour growth and proliferation. Tumours are effective in deriving the additional biomass needed for growth and proliferation from glycolysis because of the inefficiency of this pathway. Glycolysis produces numerous side products while metabolising glucose compared to oxidative phosphorylation uses all the available carbons in glucose to produce ATP [16]. This excessive production of lactate via aerobic glycolysis has implications for cellular health and homeostasis as lactate is transported out of the cells and used as biomass to further tumour growth [16].

1.2.3 Sodium in cancer

Excess production of lactate by aerobic glycolysis enables several malignant characteristics of cancerous cells. Due to the increase in proton concentration within the cell, intercellular conditions become acidic. To maintain cellular function, excess protons must be expelled from the cell. This results in extracellular acidosis as the protons begin accumulating outside of the cell. A heterogenous distribution of acidity, hypoxic conditions, and other environmental factors create the conditions to produce a highly heterogeneous tumour population that is malignant. The increase in proton concentration outside the cell has additional consequences. Various proton transport proteins are heavily involved in the extrusion process, with the most prominent being the sodium proton antiporter (NHE1), a transporter upregulated in GBM [18]. This protein can be upregulated up to 15-fold over the expression level in human neural stem cells [19]. This channel exchanges protons for sodium ions on a one-to-one ratio. Over time, this action contributes to the increase in sodium concentration within the cell due to the accumulating sodium ions.

Additionally, sodium concentration in the tumorous region can be affected by changes in the ratio between the intracellular and extracellular volume fractions. The extracellular volume fraction occupies a much smaller area than the intracellular space, but has a much higher sodium concentration [20, 21]. Increases in the extracellular volume fraction due to increased perfusion in the region, increased leaky vessels, or remodeling of the tumour micro-environment due to cancerous growth can cause overall tissue sodium concentration to also increase [21]. Overall, sodium concentration has shown to be increased in tumours and has potential to act as a biomarker for tumour growth [18, 22, 23].

1.3 Pre-clinical GBM animal models

Preclinical models are essential for the translation of research as they link the translation of *in vitro* cell based researched into clinical application and *in vivo* studies. These models allow researchers to test the applicability and translatability of their findings within a more complex system for the eventual hope of application into clinic or human settings. Preclinical models also find applicability in the testing of novel imaging modalities such as magnetic particle imaging (MPI) [24]. Evaluating and validating these new imaging modalities in preclinical models of disease lays the foundation for assessing the relevance of these new modalities for human imaging.

Translatable imaging methods require animal models which can accurately recapitulate the biological interactions and clinical progression of human disease. Depending on the topic of study, different models will reproduce different aspects of the target biology. For preclinical GBM models of human gliomas the following features are desired: an approximating genotype, similar genetic, epigenetic, and phenotypic intra-tumoral heterogeneity, and the development of a representative tumour micro-environment (including immune cell interactions, cell-cell interactions, and BBB) [25].

Animal models for the study of GBM have been developed for *in vivo* studies. The most common models used are small rodents, having multiple strains and species applicable to different purposes. Small rodent models can be generated in several ways, although cell-line derived models are the most common. Cell line-derived models rely on cancer inoculation using established, long-term *in vitro* cultured tumour cells. These cell lines can be transplanted into syngeneic hosts for allographic or xenographic (human-based) models. In addition, cell-line cancer cells can be placed either ectopically, or orthotopically in its natural tissue of origin. Preference of model, cell-line type, and location depends on which aspect of cancer biology is of interest [26]. For example, the U87 glioma is a human derived GBM cell line which has been used extensively for investigating tumour angiogenesis and anti-angiogenic therapies. However, this cell line fails to replicate key GBM phenotypes, such as diffuse infiltration, and a homogeneous appearance when imaged. Comparatively, the U251 glioma is also human derived, but better recapitulates the phenotypic aspects of GBM where U87 fails [27]. Having a cell line which can capture the genotypic and phenotypic characteristics of GBM improves the translatability of research which relies on these cell lines. Ideally, research would be conducted using patient-derived xenographs which could capture the complexities and nuances of GBM [28].

Of the available small rodent pre-clinical models, mouse models are most commonly used due to their ubiquitous use for genetic manipulation, having been used to generate a variety of immunocompromised strains which have been used with many cell-lines [29-31]. However, there are two major considerations with these models. The first applies only to immunocompromised models using human cells, where the characterization of biological behaviour may be impacted due to the lack of tumour-immune cell interactions. Implantation in immunocompetent models allows for the study of tumour immunological characteristics, whilst implanting in immunocompromised animals allows for the evaluation of immunotherapies [32]. The second limitation is due to their small size, which limits their use for certain imaging applications as the spatial resolution needed for effective imaging could impact the signal-to-noise ratio (SNR) of the modality. With magnetic resonance imaging (MRI), this limitation can be overcome using high magnetic field strengths or using custom coils and gradient hardware [27].

Pre-clinical rat models are likewise a useful tool available for cancer models. Although most of these models are allogenic cell-line based due to the difficulty of producing immunocompromised strains. The major advantages of working with rat models include the greater accuracy for tumour implantation, as well as greater physiological similarities to humans, as compared to mice [32]. Several GBM cell-line models have been developed in different rat species, with the most used lines being C6, 9L, and F98 cell-lines. The 9L gliosarcoma cell line has been the most widely used experimental rat brain tumour model, and has been used extensively to study chemotherapy and radiation therapy [27, 32]. However, considerations must be taken when using gliosarcoma as a model for GBM, as there are distinctions between the behaviour of these diseases [27, 33]. The F98 glioma cell line is more representative comparatively, replicating human glioma invasive growth patterns and gene expressions, however F98 tumours resemble anaplastic gliomas more than GBM tumours [27, 34]. Of similar comparability is the C6 glioma cell line, which will be further described in the next section.

1.3.1 C6 rat GBM models

The C6 rat GBM cell-line was developed in the late 1960s in Sweet's laboratory in adult Wistar-Furth rats though repeated administration of *N*-methylnitrosourea [27, 32]. This cell-line has been shown to have several histopathological similarities to human GBM. The cells are spindle shaped and pleomorphic with variably shaped nuclei, resembling human GBM cells [34]. Tumours generated from C6 cells in Wistar rats have been shown to have moderate foci of necrosis, with regions of focal invasion, nuclear polymorphism, and a high mitotic index [27, 34].

The C6 cell-line has several genetic similarities to human gliomas as well, demonstrating similar changes in gene expression to human brain tumours. For example, both C6 and human GBM show frequent mutations in *p16* – a common tumour suppressor heavily implicated to play a role in primary brain tumour development [27, 35]. Specifically, C6 cells have been reported to have a mutated *p16/Ckn2a/Ink4a* locus, with no expression of *p16* and *p19* adenosine diphosphate (ADP) ribosylation factor (ARF) mRNAs [36]. Some notable differences between human-gliomas and the C6 cell line include the wild type *p53* that C6 cells possess [27]. Additionally, C6 cells have lack of glial fibrillary acidic protein – a common diagnostic marker for GBM in humans [37], and variable expression of vimentin – a cytoskeleton protein that has been associated with metastatic disease and the progression of GBM [38].

Typically, C6 cells can be implanted and grown in Wistar rats, but they have been implanted in the Sprague-Dawley and Long-Evans strain without rejection [27]. However, it should be noted that C6 tumour growth in Sprague-Dawley and Long-Evans differs greatly from growth in Wistar rats, approximating brain metastasis growth behaviour with reduced infiltration and without parenchymal invasion. When implanted inside the Wistar rat, the growth pattern of C6 more closely resembles its human counterpart. In addition, the immune micro-environment of the C6 tumour resembles human GBM [34]. It is important to note there exists a level of immunogenicity in response to the tumours within Wistar rats, such that C6 cells cannot be used for assessing immunotherapies [27]. Despite this, C6 tumours are extremely well studied and have been used to study tumour growth, cell invasion and migration, tumour angiogenesis and BBB disruption. In addition to mirroring the biology, C6 cells also mirror imaging characteristics of human gliomas – making it especially useful in imaging studies [34].

1.4 Clinical imaging of GBM

Monitoring and assessing tumour progress is very important in GBM disease management and treatment. Non-invasive imaging methods for evaluating disease progression and treatment response form the basis for decisions to alter or abandon the current therapy regime for salvage therapy [39]. These methods largely consist of anatomical imaging modalities such as ^{1}H MRI, x-ray computed tomography (CT), or positron emission tomography (PET).

These modalities are used to provide insight into brain anatomy, structural abnormalities, tumour location and degree of spread, and in some cases, functionality. The current standard for brain tumour imaging is MRI, either with or without contrast enhancement, or CT if the patient is unable to undergo MR imaging (due to a pacemaker or other magnet sensitive implants) [40]. If available, PET has been recommended and used as an additional clinical diagnostic assessment tool evaluating functional characteristics of the tumour, with glucose metabolism tracers and amino acid transport tracers being used predominantly [41].

The following section describes the use of MRI for monitoring GBM in greater detail, as well as examining the advantages and challenges associated with the modality.

1.4.1 Magnetic resonance imaging

There are a variety of MRI sequences available for anatomical imaging. Two- (2D) or three-dimensional (3D) imaging data sets can be acquired with different endogenous contrasts depending on the parameters selected. Typically, T_1-weighted, T_2-weighted and contrast enhanced (CE) sequences are used to evaluate GBM as the presence of the tumour influences the image contrast by modifying the underlying tissue structure [42]. Imaging with MR provides the most value in early disease detection and guiding intervention. The gold standard for diagnosing and monitoring GBM is brain MRI. Typically, gadolinium (Gd) CE MRI is used, as glioma lesions tend to show contrast enhancement in T_1-weighted post-Gd images [43]. MR-based evaluations can provide high resolution and high contrast anatomical images with high sensitivity but limited specificity [43]. Serial imaging with MR has revealed several prognostic features which have been associated with patient survival outcomes, such as edema – associated with poor prognosis, and non-contrast enhancing tumour – associated with longer survival [42, 43]. Additionally, research into advanced MR sequences have been able to discern various features characteristic of GBM. Techniques such as diffusion weighted imaging, dynamic susceptibly contrast enhanced perfusion imaging, and MR spectroscopy have been used in research to study GBM progression and treatment response [44-46]**.**

Given the current gold standard of GBM monitoring and diagnosis, several major challenges exist. Firstly, there are numerous non-neoplastic conditions which can mimic gliomas on neuro imaging such as: brain abscesses, subacute stroke, or other inflammatory diseases. In many cases, these conditions may also mimic similar symptoms. Therefore it is essential to not solely rely on brain MR for GBM diagnoses [40]. Monitoring treatment effect on GBM using MR presents additional challenges. Pseudo-progression and pseudo-response are the major confounding factors in GBM monitoring. Pseudo-progression is what appears as an increase in contrast enhancement and/or edema without true tumour progression. The appearance of pseudo-progression is most commonly associated with MR imaging after treatment with concomitant radio- and chemotherapy with TMZ followed by disease stability or lack of clinical progression [43]. Pseudo-response is what appears as a decrease in enhancement without true anti-tumour effect and is generally associated with anti-angiogenic therapies [43]. This occurs due to reduced delivery and retention of the contrast enhancement agent in cancerous region, resulting in a decrease in contrast enhancement. It is imperative to accurately differentiate recurrent or progressive tumours from imaging artefacts and differential treatment response. Failing to identify these pseudo-phenomena can lead to premature termination of effective therapies, unnecessary surgical interventions, or the use of additional treatment agents [3]. Unfortunately, pseudo-progression is a relatively common phenomenon and has been observed in up to 50% of all patients with GBM in their first post-therapy MR scan 2-3 months following chemo-radiotherapy [47, 48]. Pseudo-progression can be induced by a variety of causes related to the treatment itself including inflammation, ischemia, and radiation-induced necrosis [3, 49]. Radiation necrosis can appear as a single "lesion" at the resection site which can appear as a recurrent tumour. In areas far from the primary tumour, necrosis can mimic multifocal lesions [49]. As this pseudo-phenomenon often presents after treatment, this limits the application of CE MRI for post-surgery evaluation, as the pooling of fluids or vascular damage results in CE that does not reflect the true disease state. Discriminating between pseudo-progression and true progression is difficult since conventional MR cannot differentiate the two. Additionally, pseudo-progression can resolve spontaneously, which can mislead observers to believe that the treatment is effective [50]. This spontaneous resolution is likely due to healing of the BBB and clearing of edema from the area which reduces CE in the region [51]. Identification of pseudo-progression is imperative as diagnosis can influence the choice to either continue with adjuvant therapy or change to a second-line therapy [39, 52]. While MRI continues to be the most accessible and powerful modality for evaluating tumour progression, such limitations necessitate development by future research.

1.4.2 The Macdonald criteria

The current most widely used guideline for evaluation of response to therapy in high grade gliomas is the Macdonald criteria [52]. The Macdonald criteria was established in the 1990s and has been widely adopted since [42]. Evaluation of glioma by the Macdonald criteria relies predominantly on 2D anatomical tumour measurements from consecutive post-Gd T_1-weighted MRI scans concurrent with clinical assessment and corticosteroid dosing [52, 53]. This allows for evaluation of neurological symptoms and the use of corticosteroids to target tumour-induced edema [54].

According to the Macdonald criteria, high grade glioma tumours are assessed based on changes in the largest cross-sectional area from consecutive post-Gd T_1-weighted images obtained at least 1 month apart [53]. The cross-sectional area measurement is obtained from the product of the largest cross-sectional diameter and the largest diameter perpendicular to it. Tumour response is classified into one of four categories: complete response (CR), partial response (PR), progressive disease (PD), and stable disease (SD). The imaging evaluation criteria for CR is the complete disappearance of enhancing disease on consecutive MRI scans at least one month apart. A classification of PR requires a greater than 50% reduction in the size of the enhancing tumour on consecutive MRI scans and no new lesions. A classification of PD requires a greater than 25% increase in the enhancing tumour size, or the appearance of new lesions. Lastly, SD consists of scenarios which do not fall into any of the above [53].

The widespread adoption of the Macdonald criteria and the advent in imaging technology and therapeutics has revealed many areas where the current measures lack specificity and sensitivity for assessing response to therapy. Specifically, the criteria have been criticized for its ambiguity for defining appropriate thresholds for lesion size and lack of detail in how to apply the criteria [42]. Critically, the scope of the Macdonald criteria does not address the challenges of pseudo-progression and pseudo-response. This is largely due to how heavily the criteria relies on Gd-enhanced images. It is also important to note the limitations inherent in the tumour measurement technique, where the maximal perpendicular diameters in the contrast enhanced tumour are used to calculate a cross-sectional area. This measurement method has limitation application in irregularly shaped tumours and can be subject to inter-observer variability [55].

Contrast enhancement in tissues relies heavily on vascular permeability. This can severely limit its applicability in non-vascularized tumours and when used in conjunction with anti-angiogenic drugs [56]. Additionally, contrast enhancement for glioma in post-treatment brain is non-specific and cannot be considered a true measurement of tumour response but rather the integrity of the BBB [52]. Enhancement can also be confounded by a variety of factors, including radiation necrosis, inflammatory response, edema in the surrounding tissues, changes in corticosteroid doses, and radiological technique. This makes changes in contrast enhancement subject to many factors and thus limits interpretation as changes in enhancing area cannot be directly equated to changes in tumour size [55].

1.4.3 Response Assessment in Neuro-Oncology

The Response Assessment in Neuro-Oncology (RANO) criteria was introduced in 2010 to address the limitations of the Macdonald Criteria [50]. While the criteria are currently largely used for clinical trials, it is the current gold standard for evaluation of pseudo-progression and improves on the Macdonald Criteria significantly. The RANO criteria introduced assessment for non-enhancing areas of the tumour and critically focused on identifying pseudo-progression [39]. The RANO criteria utilizes T_2-weighted and fluid-attenuated inversion recovery (FLAIR) imaging in addition to Gd-enhanced MR images as part of the imaging criterion for response assessment. The usage of T_2-weighted and FLAIR imaging produce tumour contrast without the use of agents and allow for identification of changes in non-enhancing areas [55].

Like the Macdonald criteria, the RANO criteria also uses the cross-sectional area produced by the maximal perpendicular diameters in the contrast enhancing area [55]. For measurable disease, the diameters must be obtained from CT or MR scans with clearly defined margins. Diameters must be at least 10mm and visible on two or more axial slices at most 5mm apart. Disease is considered unmeasurable when lesions do not have clearly defined boundaries and diameters less than 10mm. Unlike the Macdonald criteria, RANO also introduces measures for multifocal lesions – where at least the two largest lesions should be measured. In cases of high grade gliomas a maximum of five of the largest lesions should be measured [55, 56].

The RANO criteria also divides tumour response into CR, PR, PD, and SD criteria. Where basic imaging criterion for CR is defined as no enhancing disease for 4 weeks and stable or improved T_2-weighted/FLAIR visible lesions; indicated by minimal changes or reduced lesion size. Criteria for PR requires $\geq$ 50% decrease in enhancing lesion size with stable or improved T_2-weighted/FLAIR lesions and no appearance of new lesions. Criteria for PD requires a $\geq$ 25% increase in enhancing lesion size, increased T_2/FLAIR lesion size and/or appearance of any new lesions outside the radiation field [39]. There are also additional criteria for the identification of pseudo-progression [50]. Under RANO, true tumour progression within the first 12-weeks post-radiotherapy occurs if most of the new enhancement occurs outside the radiation field or with histological confirmation [3, 42]. However, practices for evaluating progression within the radiotherapy field requires MR changes to persist for at least 4 weeks before being definitively confirmed [3].

Despite the improvements RANO has made to previous criteria, limitations still exist. Although non-enhancing regions are taken into consideration using T_2-weighted and FLAIR imaging, changes in the non-enhancing regions can occur due to treatment, surgery, or radiotherapy [42]. The addition of non-contrast enhanced criteria is limited by the lack of objective imaging parameters resulting in subject interpretations and high adjudication rates [3, 56]. RANO is still limited as it still uses bidirectional measurements of contrast enhanced tumour size. This method of measurement has been shown to overestimate tumour volume and results in higher reader discordance due to the challenges of identifying the longest perpendicular diameters in irregularly shaped tumours [56]. Additional limitations are presented in the arbitrary thresholds for defining response and progression – as the use of thresholds based on percentage change from baseline are biased towards small tumours as small changes in absolute tumour size result in large percentage changes [56].

Currently, RANO still remains the gold standard for assessing tumour response in GBM. Although limited in several aspects, it improves significantly upon the previous Macdonald criteria and introduced new criteria for addressing pseudo-progression and non-contrast enhancing lesions.

1.5 Basics of magnetic resonance imaging

Magnetic resonance imaging (MRI) is a versatile modality used for medical imaging. It provides superior contrast between soft tissues compared to other modalities such as CT or ultrasound (US). MR imaging can produce 2D and 3D images with differential contrasts. This allows for identification of abnormalities or diseases that may appear differently under different imaging conditions.

Standard MRI uses a strong, homogeneous magnetic field to induce nuclear magnetization in hydrogen atoms associated with water molecules and fat in the subject. The magnetic field is generated by a superconducting magnet which can be used to generate magnetic fields on the order of Teslas (T). Comparatively, a fridge magnet averages around 1mT. Fields strength is often associated with specific imaging applications. Scanners used in clinical settings can range between 1.5T to 3T. Scanners used for research purposes can have field strengths ranging up to 21.1T [57]. However, most commonly these high-field research scanners will range from 7T to 10T [58].

This section will provide a general overview of the physics governing magnetic resonance image formation and factors affecting image contrast.

1.5.1 Nuclear spin and magnetization

The foundation of MRI relies on nuclear magnetic resonance of a nucleus of interest. Traditionally, the proton is the nucleus of choice due to its high *in vivo* concentration (80M) and high MR sensitivity due to its magnetic dipole moment [59]. Nuclei that can undergo magnetic resonance must have a non-zero spin and hence, a magnetic dipole. The magnetic dipole can be conceptualized as a free precessing bar magnet in space. Typically, these magnetic dipoles are randomly oriented, resulting in a net-zero magnetization as the magnetization cancels over the volume for a large ensemble. However, in the presence of a large external magnetic field ($\overrightarrow{B_0}$) – such as the field generated by an MRI, the magnetic dipoles precess around $\overrightarrow{B_0}$. The distribution of angles in the cone of precession is almost uniformly distributed between 0° and 180°, with a slight preference for smaller angles with increasing field strength. This results in a net magnetization ($\overrightarrow{M_0}$) which underlies the source of the MR signal (Figure 1-1.) [60].

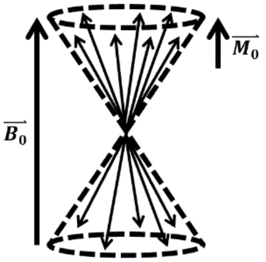

Figure 1-1. Illustrative schematic showing orientation of magnetic dipoles in the presence of a large external magnetic field ($\overrightarrow{B_0}$). Magnetic dipoles preferentially align in the direction of the large magnetic field resulting in a net magnetization ($\overrightarrow{M_0}$).

By convention, the direction of $\overrightarrow{B_0}$ is used to define the Z-axis of a Cartesian coordinate system. The rate of precession of the protons for a given $\overrightarrow{B_0}$ depends on the nucleus of interest and the strength of B_0 and is described by the Larmor frequency (ω_0) as defined by equation 1.1 [59].

$$\omega_0 = \bar{\gamma}B_0 \tag{1.1}$$

Where $\bar{\gamma}$ is the gyromagnetic ratio; an intrinsic characteristic of MR sensitive nuclei which describes the magnetic dipole strength. The gyromagnetic ratio for some common nuclei is listed below in Table 1-1**.**

Nucleus	Gyromagnetic ratio (MHz/T)
^{1}H	42.575
^{19}F	40.078
^{23}Na	11.262

Table 1-1. Gyromagnetic ratios ($\bar{\gamma}$) of some commonly imaged nuclei. Of these, ^{1}H is the most imaged nucleus, with the largest $\bar{\gamma}$) value.

The $\overrightarrow{M_0}$ of a volume can be affected by several factors. Including the number of magnetic nuclei per unit volume, the magnetic moment of these nuclei (as described by $\bar{\gamma}$), and $\overrightarrow{B_0}$. MRI is practically limited by the sample magnetization which limits the speed of image acquisition and achievable image resolution. Imaging of hydrogen protons is ultimately made feasible by the combination of these factors as the concentration of protons in soft tissue is approximately 80M and 62% of all nuclei in the body are protons [59]. Moreover, imaging of non-hydrogen nuclei (X-nuclei) must overcome these challenges to present with useful MR signals. These challenges will be detailed further in section 1.6.

To detect MR signal, $\overrightarrow{M_0}$ must first be rotated away from its position along the Z-axis through the action of a second oscillating magnetic field ($\overrightarrow{B_1}$) generated by a transient radiofrequency (RF) pulse. This field oscillates at the Larmor frequency in the XY plane perpendicular to the Z-axis. The B_1 field excites or "tilts" $\overrightarrow{M_0}$ away from the Z-axis to some desired angle, after which is it turned off. The angle that $\overrightarrow{M_0}$ is tilted is known colloquially as the flip angle (α). For example, for an α of 90°, $\overrightarrow{M_0}$ would rest completely in the XY plane. Following the transient RF excitation $\overrightarrow{M_0}$ will begin to relax or "decay" back to its original position along the Z-axis. The amplitude of the magnetizations' projected components over time characterize different relaxation profiles. The amplitude of the magnetization in the XY-plane decays from a maximum to a minimum, while the amplitude of the magnetization along the Z direction recovers back to its original value. The decay of the magnetization in the XY plane and the regrowth of the magnetization along the Z-axis are known as the transverse and longitudinal relaxations respectively. Contrasts between tissues in MR relies on the differences in relaxation profiles from different tissues [59]. These concepts of relaxation, contrast, and signal detection will be further expanded upon in following sections.

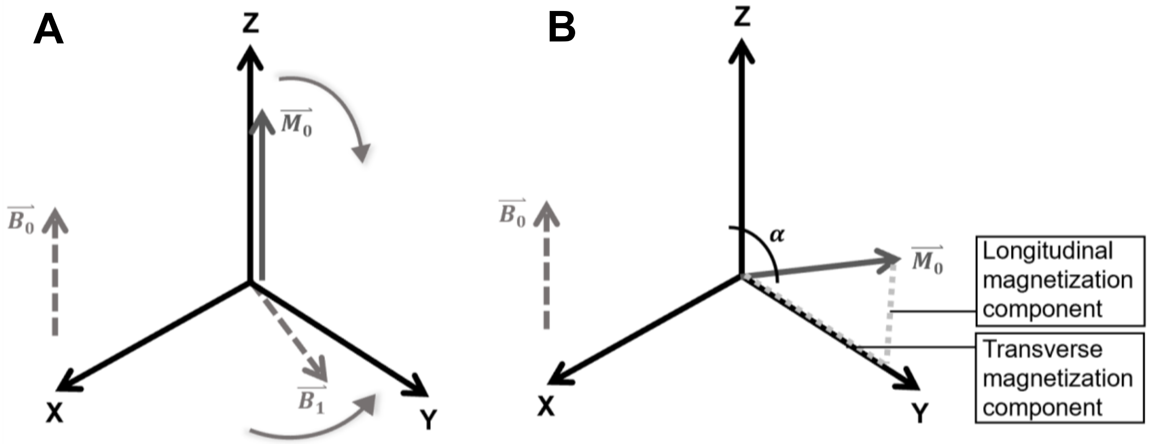

Figure 1-2. Illustrative schematic showing the behaviour of the net magnetization ($\overrightarrow{M_0}$) under **(A)** excitation by an external field ($\overrightarrow{B_0}$). Grey arrows show the direction of movement of the $\overrightarrow{B_1}$ and $\overrightarrow{M_0}$. **(B)** Shows the behaviour of $\overrightarrow{M_0}$ after being tilted away from the main magnetic field ($\overrightarrow{B_0}$). Dotted lines show the longitudinal and transverse magnetization components of $\overrightarrow{M_0}$ and α shows the flip angle of $\overrightarrow{M_0}$.

1.5.2 Transverse magnetization and relaxation

The transverse magnetization is the component of $\overrightarrow{M_0}$ projected into the XY plane. This magnetization holds its largest amplitude immediately after all the magnetization has been flipped into the transverse plane after an α of 90°. Over time, this component will decay to zero as $\overrightarrow{M_0}$ precesses around $\overrightarrow{B_0}$. This decay is exponential with time, t and is described by equation 1.2

$$M_t = M_t(0)e^{-\frac{t}{T_2}} \tag{1.2}$$

Where T_2 is the transverse relaxation time constant, an intrinsic characteristic of the material being imaged. *In vivo*, T_2 values are tissue specific and can differ based on tissue type and composition [59, 61].

Transverse relaxation (also known as spin-spin relaxation) occurs due to a dephasing of the precessional phases of individual constituent magnetic dipoles in the tissue. This reduces the net amplitude of the transverse magnetization. Dephasing occurs more rapidly in a non-uniform magnetic field as different field strengths occurring across an imaging voxel will result in different local precessional frequencies. The T_2^*, also known as the effective T_2 accounts for this field inhomogeneity and is also affected by other external factors such as system imperfections, tissue/air (or tissue/metal) interfaces, and blood oxygen levels. This effective T_2 is always shorter than the intrinsic T_2 value of tissue [59]. The impact of T_2^* can be overcome through MR sequence design, particularly by using the spin echo sequence which will be further described in section 1.5.6.

1.5.3 Longitudinal magnetization and relaxation

The longitudinal magnetization is the component of $\overrightarrow{M_0}$ along the Z-axis. Overtime, this component exponentially grows from a minimum back to the original $\overrightarrow{M_0}$ value. This growth can be characterized by the following equation [61].

$$M_z(t) = M_0\left(1 - e^{-\frac{t}{T_1}}\right) \tag{1.3}$$

Here T_1 is the longitudinal relaxation (also known as the spin-lattice relaxation) time constant, or the characteristic time taken for the magnetization vector to realign with the direction of B_0. When $\overrightarrow{M_0}$ has been tilted to 90^o, the longitudinal magnetization component is zero, but begins to grow back through longitudinal relaxation. Like transverse relaxation, longitudinal relaxation rates differ depending on the tissue. By convention, the T_1 value of a specific tissue is defined as the time taken for the longitudinal relaxation to reach 63% of its final value assuming a 90^o pulse is used [59].

1.5.3.1 T_1 contrast agents

T_1 contrast agents find their use in MR imaging by increasing the specificity of MR contrast. These agents have magnetic properties which manipulate the T_1 of tissue in their vicinity and increases the differences in signal between tissues at specific T_1 times. Contrast enhancement occurs due to shortening of the targeted tissue's T_1 values. This increases the signal of the target tissue while the background signal remains the same when imaged with a MR sequence with T_1 contrast weighting. Enhanced relaxation occurs due to strong dipole interactions between the proton magnetic dipole moment and that of unpaired electrons in the contrast agent. Contrast agents with unpaired electrons are paramagnetic and are typically lanthanide compounds (such as gadolinium) which require chelation due to concerns over metal toxicity. The chelation allows the hydrogen protons in water molecules to get close to the paramagnetic agent for dipole-dipole interactions but prevents absorption of the toxic agent within the body. Gd-based contrast agents are typically delivered through an IV bolus with arterial enhancement lasting for a few minutes. Generally, the contrast is non-specific and could depend on the vascular perfusion in the region of interest [58, 62].

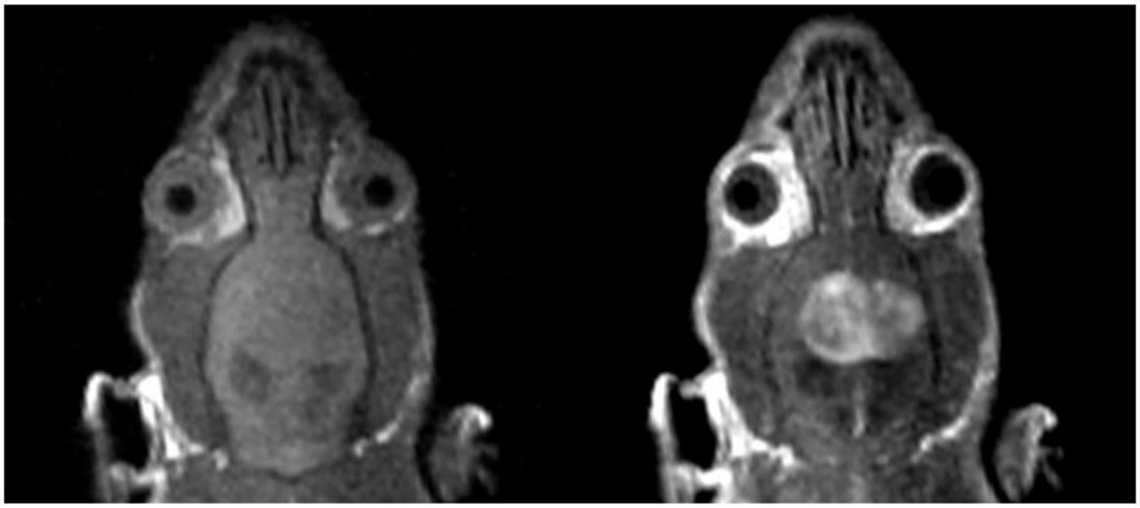

Figure 1-3. Pre (L) and post (R) gadolinium contrast enhanced images of the rat head from a coronal view. Enhancement can clearly be seen in the region of the tumour and in the region surrounding the eyeballs.

1.5.4 T_1 and T_2 weighted imaging

The intrinsic differences among T_1 or T_2 values in different tissues underlies the ability of MRI to distinguish soft tissues. Sequence design for MR imaging takes advantage of these differences to produce images with different contrasts. The typical MRI sequence consists of a series of RF pulses repeated over time, known as a pulse sequence. In a standard pulse sequence, there is a specified period between RF excitation and when signal acquisition begins. This time is known as time-to-echo, or TE. This gives the tilted $\overrightarrow{M_0}$ a period to relax. As mentioned above, this relaxation occurs at different rates for different tissues *in vivo*. Ideally, when signal acquisition begins, the differences between the magnetization of different tissues are maximized, generating contrast between them. Optimal choices for TE depend on the contrast weighting of the image, and the area being imaged. An additional factor to consider is the time between each pulse sequence repetition, known as the time-to-repeat or TR. This is the time between each excitatory RF pulse. Adjusting this time allows for the magnetization to relax to a desired state before repeating the pulse sequence. Variation of TE and TR provide the basic methods to adjust image contrast. T_1-weighted images can be obtained using pulse sequences with short TEs and short TRs. Under this contrast, fluids will typically appear darker while fattier tissues will appear brighter. T_{2}-weighted images can be obtained with long TEs and long TRs. Under this contrast, fluids will typically appear brighter and fats tissue will appear darker [59].

1.5.5 Spin-density weighted imaging

A less commonly imaged MR weighting is spin-density weighted imaging, also known as proton density or nuclear density weighted imaging. In this weighting, the contrast between tissues relies solely on the number of magnetically resonant nuclei within the volume and tissue of interest. This produces contrast that is proportional to the concentration of nuclei. With brighter areas having more MR sensitive nuclei than darker areas. These images can be obtained using pulse sequences with long TRs and short TEs. The long TR allows the T_1 of the tissue to recover to the original value, removing T_1 effects. The short TE minimizes T_2 effects as decay is minimized [59, 62]. In X-nuclear imaging, this spin-density weighting can be achieved by modifying sequences to have TRs and TEs that reflect the T_1 and T_2 values of those nuclei in tissues. This provides a method to interrogate the concentration of the X-nucleus within the volume of interest. This type of X-nuclei imaging has been used to investigate ^{19}F and ^{23}Na *in vivo* as molecular imaging probes [13, 63].

1.5.6 Spin echo imaging

The spin echo pulse sequence is a versatile sequence which uses a 90° excitatory RF pulse followed by at least one 180° pulse. This sequence can be used to produce spin density, T_1-, and T_2-weighted images. The main characteristic of the spin echo is the 180° "refocusing" pulse. This pulse results in rephasing of the transverse relaxation components into an "echo" allowing for more signal acquisition. For a conventional spin echo sequence at 1.5T, typical parameters for T_1-weighted images are TE=20ms and TR=500ms. Typical parameters for T_2-weighted images are TE=80ms and TR=2000ms [59].

Fast spin echo (FSE) imaging improves on the conventional spin echo sequence by reducing scan time. This is done by repeating the 180° refocusing pulse with signal acquisition following each inversion, allowing for multiple readouts to be obtained within one TR. The echo train length (ETL) parameter describes how many echoes are to be acquired in one TR, with imaging time inversely proportional to ETL. The rapid imaging achievable by FSE and the ability to produce many different image weightings make FSE one of the most useful MR pulse sequences [62].

1.5.7 Introduction to RF technology

The main tool for MR imaging is the RF coil. These coils are the source of the excitatory RF energy as well as the tool for receiving the MR signal. Transmit (Tx) coils are designed to generate a uniform oscillating electromagnetic field. Most often, this is the RF coil incorporated within the MRI bore known as the body coil. To transmit RF energy to excite a particular nucleus, Tx coils must produce an electromagnetic field that oscillates at or near ω_0 for that nucleus. Additionally, the field must oscillate in a plane perpendicular to the main field of the magnet to facilitate excitation of $\overrightarrow{M_0}$. The amount of RF energy required to excite a particular nucleus is determined through the transmit gain (TG). This parameter determines how much energy is needed to induce a 90° flip angle and is used to calibrate all other flip angles specified. Values for TG can depend on the subject imaged, coil type, and sequence used. Often, the excitatory RF pulse is transmitted by one coil, and the resultant MR signal is received by another coil. This allows for simpler RF coil designs and when used together with transmission by the body coil of the MRI, allows for more uniform excitation over the entire volume. However, it is also possible for a single coil to serve both the Tx and receive (Rx) functions. This type of coil can reduce whole body exposure to RF induced heating, allows for acquisition of more slices, and reduces artefacts from tissues outside the volume of interest. Challenges that face Tx/Rx coils are the more complex coil designs required, and reduced B_1 field uniformity over the volume of interest [62, 64].

The resonant frequency of the RF coil depends on the inductance (L) and capacitance (C) of the components in the circuit. This is the frequency where the coil works most efficiently for RF transmission and/or reception. Typically, the resonant frequency of the coil can be tuned by adjusting capacitors placed along the conducting loop. Tuning ensures that the coil efficiently responds to signal over a very specific frequency range. The simplest Rx coil consists solely of a loop of copper wire tuned to the Larmor frequency of the nucleus of interest at a specific field strength. As seen in equation 1.1, ω_0 depends on the main field of the magnet, meaning a hydrogen proton in a 3T system precesses at a different frequency from a hydrogen proton in a 1.5T system or any other MR-visible nucleus at the same field strength [58, 62].

Coils are available in a variety of geometries which can serve different imaging needs. The most common are birdcage coils, surface coils, and solenoids. Birdcage coils and surface coils will be discussed in greater detail. Of these geometries, the birdcage coils are perhaps the most ubiquitous owing to their versatility and reliability. This coil geometry can be used for Tx/Rx and creates a uniform excitation and SNR within its bore, making it very useful for 3D imaging. The surface coil has the simplest geometry and can often exist as a simple loop. This type of coil can be used to interrogate very specific regions of the body, and as this coil is able to be shaped to the region of interest, an SNR increase can be observed as noise from outside of the sampled area is filtered [64]. However, this comes at the cost of imaging volume and signal falls off as distance from the surface of the coil increases. Surface coils perform best when the coil size is close to the size of the imaged object. Unfortunately, its 2D geometry results in a non-uniform receive profile. Images produced from a surface coil tend to have high SNR near the coil surface with rapid signal fall off as distance from the coil increases. Correction pipelines are often used to correct for non-uniformity in images from surface coils [65]**.** Surface coils can be arranged into an array, which extends the volume of useable SNR of a single small surface coil. This allows for imaging with a surface coil with high sensitivity over a larger volume [62].

There are additional challenges faced by surface coils with Tx/Rx capabilities. When setting TG in surface coils, the spatial inhomogeneity of the emitted RF energy presents a major challenge. Due to the asymmetry of excitation, as RF energy increases, the region in the coil where nuclei are flipped 90° shifts throughout the sample volume. This can be ameliorated with a reference marker and shift reagent. A shift reagent is a molecule which can affect the magnetic field experienced by certain nuclei, and thereby shift the precession frequency of that nucleus. The amount of frequency shift the nuclei experiences depends on the reagent and its concentration in the solution with the nuclei of interest. Frequency shifts to the tune of a thousand Hz are possible [66]. When an RF coil tuned to a specific nucleus is used on a subject and a shift reagent solution, two MR signal peaks will be detected. One peak will belong to the ω_0 of the nuclei within the subject, while the other peak results from the impact of the shift reagent. If this shifted peak is distinct and well resolved from the subject peak, it can be used as a reference for setting the RF energy input into the system. By placing the shift reagent solution in a known and consistent position, RF energy input can be evaluated for this reference point across multiple imaging sessions. When used in conjunction with a surface coil, reproducible excitation profiles can be generated [64, 66].

Despite different coil geometries, MR signal is usually received in the same way. After excitation, the resulting precessing transverse magnetization induces a voltage in the RF coil. This voltage oscillates at the Larmor frequency with an amplitude that decays exponentially with a time constant given by T_2*. It is this voltage signal that is amplified by the receive channel and passed on to a computer for processing into an MR image [62].

1.6 Sodium magnetic resonance imaging

As discussed previously in section 1.2, tissue sodium levels are significantly impacted in cancer and other diseases. Sodium is one of the two endogenous nuclei suitable for human MRI [21]. Changes in total tissue sodium concentration (TSC) as measured by sodium MRI (^{23}Na MRI) are more sensitive to disease changes on the molecular level in conditions like cancer, stroke, or multiple sclerosis compared to proton MRI [67]. This section will provide background on the techniques and challenges associated with imaging sodium using MRI.

1.6.1 Sodium MRI

Nuclei suitable for MRI require a magnetic dipole moment formed from a non-zero spin value. Sodium fulfills this requirement as all sodium nuclei have a nuclear spin of $\frac{3}{2}$, allowing it to present a detectable MR signal. However, the nature of the sodium nucleus presents challenges specific to its nuclear characteristics. Magnetic resonance signals also depend on $\bar{\gamma}$ and the *in vivo* concentration of a nucleus. The signal in MRI is approximately proportional to γ^3. Given that the $\bar{\gamma}$ of sodium is only 11.262MHz T^{-1} compared to 42.577MHz T^{-1} for ^{1}H, the available sodium signal is significantly less than the available proton signal. Additionally, the average *in vivo* TSC between the intra- and extracellular environments is approximately 40mM [67]. Comparatively, the average concentration of water-associated protons is 80M. Combined, these factors make the sodium signal much smaller and more difficult to detect compared to proton (~30,000 times lower) [14]. However, nearly 100% of sodium *in vivo* exists as the MR sensitive isotope, meaning most of the biologically available sodium contributes to the detected sodium signal [13].

Additionally, the $\frac{3}{2}$ nuclear spin has implications for the behaviour of the sodium signal. In addition to a magnetic dipole moment, sodium has an electric quadrupolar moment that interacts strongly with the electric field gradients in its environment. In addition to dipole interactions, these quadrupolar interactions cause the sodium nucleus to exhibit biexponential T_2 relaxation. The T_2 relaxation of sodium has a slow component ($T_{2,\text{slow}}$ ~15–30ms) and a fast component ($T_{2,\text{fast}}$ ~1–5ms) owing to its biexponential nature. The T_1 relaxation of sodium is mono-exponential but is also rapid at ~30-40ms [14]. The range of these relaxation values also depends on the tissue of interest. Within the brain, white matter and grey matter have relaxation times that differ from cerebral spinal fluid (CSF) [13]. These relaxation values are listed in Table 1-2.

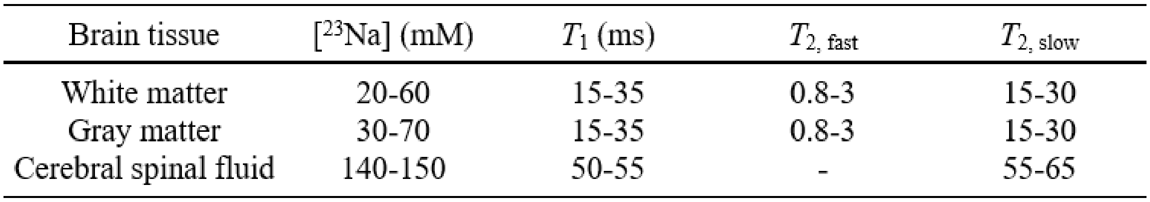

Brain tissue	[^{23}Na] (mM)	T_1 (ms)	$T_{2,\text{ fast}}$	$T_{2,\text{ slow}}$
White matter	20-60	15-35	0.8-3	15-30
Gray matter	30-70	15-35	0.8-3	15-30
Cerebral spinal fluid	140-150	50-55	-	55-65

Table 1-2. Sodium relaxation times for human brain tissues *in vivo.* These ranges are based on references [13, 68, 69] and references within.

To maximize acquired sodium signal, ^{23}Na MRI requires specialized hardware and software. Custom RF coils tuned to the ω_0 of sodium and an MR system fitted with broadband transcieve capabilities are required to image sodium. In addition, sequences for sodium require ultrashort echo times (UTE) less than 0.5ms. These sequences also typically acquire at low resolutions with short excitation RF pulses to minimize sodium signal loss and maximize SNR [70]. Overall, sodium imaging sequences require longer acquisition times and more averages to obtain high SNR. However, there are technical limits regarding how long a subject can be imaged due to subject motion and equipment stability. Therefore, efficient sequence design is necessary for clinical applications. Details regarding ^{23}Na MRI sequences will be expanded in the following section.

1.6.2 Sodium imaging sequences

Sodium imaging sequences prioritize maximizing SNR to overcome the inherent limitations of imaging sodium *in vivo*. MR sequences designed with UTE in mind aim to avoid the short T_2 effects associated with the sodium nucleus and allows for quantitative ^{23}Na MRI [21]. Ideally, this TE needs to be shorter than 0.5ms to detect both T_2 components of sodium [13]. One of the methods used to minimize TE is the adoption of a radial *k*-space encoding scheme rather than Cartesian. In Cartesian *k*-space encoding, a phase encoding gradient and frequency encoding gradient are required, which in essence allow the MR signal to be read out across the plane line by line. However, there is no signal acquisition during the time needed for the phase encoding gradient – resulting in undesirable losses in SNR when imaging sodium.

Sodium imaging sequences like 3D projection reconstruction (3DPR) and twisted projection imaging (TPI) use a radial encoding scheme. These methods apply a short, hard excitation pulse, followed by radial gradient trajectories to acquire from angular projections (3DPR) or spiraled trajectories (TPI). The 3D encoding gradient eliminates the need for phase encoding gradients as the MR signals can be read outwards from a central point. These sequences are able to shorten TE significantly compared to phase encoded sequences [21]. A traditional 3DPR imaging scheme relies on these constant radial projections to fill in *k*-space. However, it's limited by over-sampling in the central regions of *k*-space (low-spatial frequency) and under-sampling in the edge regions of *k*-space (high-spatial frequency) which can result in blurring [21, 71]. The TPI imaging scheme overcomes this limitation of 3DPR. Rather than reading the MR signal out in straight lines from center out, the readouts for this scheme follow varied spiral like trajectories to uniformly sample *k*-space producing high SNR images. However, TPI is limited by its complex implementation and high hardware demands [21, 70].

A different imaging scheme that is based on 3DPR is the density-adapted 3DPR (DA3DPR) sequence. This sequence can match the SNR efficacy of TPI without the hardware demands. The main improvement DA3DPR makes on traditional 3DPR imaging is overcoming the non-uniform *k*-space sampling. Ultimately this sequence requires many trajectories to fully cover all of *k*-space to satisfy the Nyquist sampling criterion. Overall DA3DPR imaging has been demonstrated to acquire images with increased SNR and reduced blurring [72].

1.6.3 Tissue sodium concentration

There are different ways to interpret the sodium MR signal, with considerations for each. The sodium signal can be measured quantitatively, either as TSC or the intracellular sodium concentration, given as an absolute sodium concentration measurement in mM [21]. The intracellular concentration is of particular interest because of its sensitivity to cell viability and ion homeostasis, which are implicated in disease states in neurodegenerative diseases [14]. TSC is a weighted average of the intracellular and extracellular sodium compartments [67]. This is different from obtaining measurements of the intracellular sodium concentration specifically. Isolating sodium compartments requires significant post-processing of the images and multiple image acquisitions [14].

It is also possible to quantify the sodium signal by looking at changes in the signal intensity. However, this method has some limitations owning to possible differences between acquisitions as signals can be confounded by non-uniform spatial distributions of the flip angle (α). Therefore, maintaining the same spatial distribution of α between scans is important for accurate measurements [21]. Ultimately these methods of sodium quantification are possible as they are based on spin-density weighted imaging, made possible by sodium sequence designs.

1.7 Project aims and hypothesis

The aim of this thesis was to conduct a preliminary study investigating treatment effects using sodium MRI. A DA3DPR sodium imaging sequence was implemented for quantitative small animal imaging at 3T and ^{23}Na MRI for examining longitudinal treatment response in pre-clinical models of GBM was investigated. Implementation and optimization of the DA3DPR sequence for quantitative small animal sodium imaging was evaluated using a curved butterfly surface coil. The optimized sequence and imaging protocol were used to evaluate longitudinal changes in TSC in a preclinical rat model of GBM. Proton (T_2, pre- and post-contrast T_1) and sodium images were acquired and co-registered to evaluate changes in tumour growth and total tissue sodium concentration over time.

It was hypothesized based on the biological relevance of sodium in tumour biology, that significant changes in TSC would be observed in response to treatment with TMZ. Treatment with TMZ can affect sodium levels in tumours through cell death – which can either result in decreased sodium levels due to a reduction in the Warburg effect, or increased sodium levels due to increases in the extracellular volume fraction [20, 73]. Specifically, it was hypothesized that TSC in the tumour region would decrease with treatment due to the decrease in metabolism. It is important to recognize that the DA3DPR sequence used for this imaging is only sensitive to total TSC and cannot differentiate between intracellular and extracellular compartments. Therefore, the expected changes would be dependent on the combined changes of sodium concentration within the cells and in the surrounding extracellular space.

The goal of this work was to investigate the potential for sodium as an MR biomarker for tumour response that could be more specific than current clinical criteria. This could potentially improve on the challenges faced when imaging GBM and the impact these challenges have on treatment and patient response.

1.7.1 Challenges of COVID-19

Over the last 16 months, we have been faced with unprecedent challenges in the form of the COVID-19 global pandemic which greatly impacted our ability to conduct pre-clinical research. In addition to delays caused by research shutdowns, many new obstacles with regards to accessing resources and personnel needed for experimental procedures arose after we recovered from the first wave. From new scheduling systems for space access to difficulties booking training sessions¸ many factors contributed to challenging progress. This thesis was ultimately able to be brought to fruition with the support of the Animal Care and Veterinary Services team in the middle of the pandemic. Additionally, support provided by fellow lab members, my supervisor, as well as the university helped to overcome the challenges and limitations imposed on us by the pandemic.

1.8 References for Chapter 1

1. Daniel, P., et al., *Temozolomide Induced Hypermutation in Glioma: Evolutionary Mechanisms and Therapeutic Opportunities.* Front Oncol, 2019. **9**: p. 41.
2. Brenner, D.R., et al., *Projected estimates of cancer in Canada in 2020.* Canadian Medical Association Journal, 2020. **192**(9): p. E199-E205.
3. Khan, M.N., et al., *High-grade glioma management and response assessment-recent advances and current challenges.* Current oncology (Toronto, Ont.), 2016. **23**(4): p. e383-e391.
4. Walker, E.V., F.G. Davis, and C.f. affiliates, *Malignant primary brain and other central nervous system tumors diagnosed in Canada from 2009 to 2013.* Neuro-oncology, 2019. **21**(3): p. 360-369.
5. Young, R.M., et al., *Current trends in the surgical management and treatment of adult glioblastoma.* Ann Transl Med, 2015. **3**(9): p. 121.
6. Holland, E.C., *Glioblastoma multiforme The terminator.* PNAS, 2000. **97**(12): p. 6242–6244
7. Ostrom, Q.T., et al., *CBTRUS Statistical Report: Primary Brain and Central Nervous System Tumors Diagnosed in the United States in 2007–2011.* Neuro-Oncology, 2014. **16**(suppl_4): p. iv1-iv63.
8. Gallego, O., *Nonsurgical treatment of recurrent glioblastoma.* Curr Oncol, 2015. **22**(4): p. e273-81.
9. Koshy, M., et al., *Improved survival time trends for glioblastoma using the SEER 17 population-based registries.* J Neurooncol, 2012. **107**(1): p. 207-12.
10. AF., T. and J. M., *Epidemiology and Outcome of Glioblastoma.* Glioblastoma [Internet], 2017.
11. Stupp, R., et al., *Effects of radiotherapy with concomitant and adjuvant temozolomide versus radiotherapy alone on survival in glioblastoma in a randomised phase III study: 5-year analysis of the EORTC-NCIC trial.* Lancet Oncol, 2009. **10**(5): p. 459-66.
12. Terry, J., *The major electrolytes: sodium, potassium, and chloride.* J Intraven Nurs, 1994. **17**(5): p. 240-7.
13. Madelin, G., et al., *Sodium MRI: methods and applications.* Progress in nuclear magnetic resonance spectroscopy, 2014. **79**: p. 14-47.
14. Madelin, G., et al., *A method for estimating intracellular sodium concentration and extracellular volume fraction in brain in vivo using sodium magnetic resonance imaging.* Scientific reports, 2014. **4**: p. 4763-4763.
15. Orlowski, J. and S. Grinstein, *Na+/H+ exchangers of mammalian cells.* J Biol Chem, 1997. **272**(36): p. 22373-6.
16. Vander Heiden, M.G., L.C. Cantley, and C.B. Thompson, *Understanding the Warburg effect: the metabolic requirements of cell proliferation.* Science, 2009. **324**(5930): p. 1029-33.
17. Warburg, O., F. Wind, and E. Negelein, *The metabolism of tumors in the body* J Gen Physiol, 1927. **8**(6): p. 519-530.
18. Stock, C. and S.F. Pedersen, *Roles of pH and the Na(+)/H(+) exchanger NHE1 in cancer: From cell biology and animal models to an emerging translational perspective?* Semin Cancer Biol, 2017. **43**: p. 5-16.

19. Cong, D., et al., *Upregulation of NHE1 protein expression enables glioblastoma cells to escape TMZ-mediated toxicity via increased H^+ extrusion, cell migration and survival.* Carcinogenesis, 2014. **35**(9): p. 2014-2024.
20. Olde Engberink, R.H.G., V. Selvarajah, and L. Vogt, *Clinical impact of tissue sodium storage.* Pediatric Nephrology, 2020. **35**(8): p. 1373-1380.
21. Bottomley, P.A., *Sodium MRI in Man: Technique and Findings*, in *eMagRes*. 2012. p. 353-366.
22. Schepkin, V.D., et al., *Proton and sodium MRI assessment of emerging tumor chemotherapeutic resistance.* NMR in biomedicine, 2006. **19**(8): p. 1035-1042.
23. Madelin, G. and R.R. Regatte, *Biomedical applications of sodium MRI in vivo.* Journal of magnetic resonance imaging : JMRI, 2013. **38**(3): p. 511-529.
24. Kaul, M.G., et al., *Combined Preclinical Magnetic Particle Imaging and Magnetic Resonance Imaging: Initial Results in Mice.* Rofo, 2015. **187**(5): p. 347-52.
25. Lenting, K., et al., *Glioma: experimental models and reality.* Acta neuropathologica, 2017. **133**(2): p. 263-282.
26. Gengenbacher, N., M. Singhal, and H.G. Augustin, *Preclinical mouse solid tumour models: status quo, challenges and perspectives.* Nat Rev Cancer, 2017. **17**(12): p. 751-765.
27. Jacobs, V.L., et al., *Current review of in vivo GBM rodent models: emphasis on the CNS-1 tumour model.* ASN neuro, 2011. **3**(3): p. e00063-e00063.
28. Lai, Y., et al., *Current status and perspectives of patient-derived xenograft models in cancer research.* J Hematol Oncol, 2017. **10**(1): p. 106.
29. Miyai, M., et al., *Current trends in mouse models of glioblastoma.* J Neurooncol, 2017. **135**(3): p. 423-432.
30. Kijima, N. and Y. Kanemura, *Mouse Models of Glioblastoma*, in *Glioblastoma*, S. De Vleeschouwer, Editor. 2017, Codon Publications Copyright: The Authors.: Brisbane (AU).
31. Jin, K., et al., *Patient-derived human tumour tissue xenografts in immunodeficient mice: a systematic review.* Clin Transl Oncol, 2010. **12**(7): p. 473-80.
32. Barth, R.F. and B. Kaur, *Rat brain tumor models in experimental neuro-oncology: the C6, 9L, T9, RG2, F98, BT4C, RT-2 and CNS-1 gliomas.* J Neurooncol, 2009. **94**(3): p. 299-312.
33. Louis, D.N., et al., *The 2016 World Health Organization Classification of Tumors of the Central Nervous System: a summary.* Acta Neuropathol, 2016. **131**(6): p. 803-20.
34. Giakoumettis, D., A. Kritis, and N. Foroglou, *C6 cell line: the gold standard in glioma research.* Hippokratia, 2018. **22**(3): p. 105-112.
35. Moulton, T., et al., *MTS1/p16/CDKN2 lesions in primary glioblastoma multiforme.* Am J Pathol, 1995. **146**(3): p. 613-9.
36. Schlegel, J., et al., *The p16/Cdkn2a/Ink4a gene is frequently deleted in nitrosourea-induced rat glial tumors.* Pathobiology, 1999. **67**(4): p. 202-6.
37. Jung, C.S., et al., *Serum GFAP is a diagnostic marker for glioblastoma multiforme.* Brain, 2007. **130**(Pt 12): p. 3336-41.

38. Zhao, J., et al., *High Expression of Vimentin is Associated With Progression and a Poor Outcome in Glioblastoma.* Appl Immunohistochem Mol Morphol, 2018. **26**(5): p. 337-344.
39. Whitton, A., et al., *Evaluation of pseudoprogression in patients with glioblastoma.* Neuro-Oncology Practice, 2016. **4**(2): p. 120-134.
40. Omuro, A. and L.M. DeAngelis, *Glioblastoma and other malignant gliomas: a clinical review.* Jama, 2013. **310**(17): p. 1842-50.
41. Verger, A. and K.J. Langen, *PET Imaging in Glioblastoma: Use in Clinical Practice*, in *Glioblastoma*, S. De Vleeschouwer, Editor. 2017, Codon Publications Copyright: The Authors.: Brisbane (AU).
42. Upadhyay, N. and A.D. Waldman, *Conventional MRI evaluation of gliomas.* The British journal of radiology, 2011. **84 Spec No 2**(Spec Iss 2): p. S107-S111.
43. Ryken, T.C., et al., *The role of imaging in the management of progressive glioblastoma : a systematic review and evidence-based clinical practice guideline.* J Neurooncol, 2014. **118**(3): p. 435-60.
44. Yoo, R.-E. and S.H. Choi, *Recent Application of Advanced MR Imaging to Predict Pseudoprogression in High-grade Glioma Patients.* Magnetic resonance in medical sciences : MRMS : an official journal of Japan Society of Magnetic Resonance in Medicine, 2016. **15**(2): p. 165-177.
45. Yamasaki, F., et al., *Advantages of high b-value diffusion-weighted imaging to diagnose pseudo-responses in patients with recurrent glioma after bevacizumab treatment.* Eur J Radiol, 2012. **81**(10): p. 2805-10.
46. Zonari, P., P. Baraldi, and G. Crisi, *Multimodal MRI in the characterization of glial neoplasms: the combined role of single-voxel MR spectroscopy, diffusion imaging and echo-planar perfusion imaging.* Neuroradiology, 2007. **49**(10): p. 795-803.
47. Pouleau, H.B., et al., *High levels of cellular proliferation predict pseudoprogression in glioblastoma patients.* Int J Oncol, 2012. **40**(4): p. 923-8.
48. Taal, W., et al., *Incidence of early pseudo-progression in a cohort of malignant glioma patients treated with chemoirradiation with temozolomide.* Cancer, 2008. **113**(2): p. 405-10.
49. Zikou, A., et al., *Radiation Necrosis, Pseudoprogression, Pseudoresponse, and Tumor Recurrence: Imaging Challenges for the Evaluation of Treated Gliomas.* Contrast media & molecular imaging, 2018. **2018**: p. 6828396-6828396.
50. Chinot, O.L., et al., *Response assessment criteria for glioblastoma: practical adaptation and implementation in clinical trials of antiangiogenic therapy.* Current neurology and neuroscience reports, 2013. **13**(5): p. 347-347.
51. Parvez, K., A. Parvez, and G. Zadeh, *The diagnosis and treatment of pseudoprogression, radiation necrosis and brain tumor recurrence.* International journal of molecular sciences, 2014. **15**(7): p. 11832-11846.
52. Hygino da Cruz, L.C., Jr., et al., *Pseudoprogression and pseudoresponse: imaging challenges in the assessment of posttreatment glioma.* AJNR Am J Neuroradiol, 2011. **32**(11): p. 1978-85.
53. Macdonald, D.R., et al., *Response criteria for phase II studies of supratentorial malignant glioma.* J Clin Oncol, 1990. **8**(7): p. 1277-80.

54. Dietrich, J., et al., *Corticosteroids in brain cancer patients: benefits and pitfalls.* Expert review of clinical pharmacology, 2011. **4**(2): p. 233-242.
55. Wen, P.Y., et al., *Updated response assessment criteria for high-grade gliomas: response assessment in neuro-oncology working group.* J Clin Oncol, 2010. **28**(11): p. 1963-72.
56. Ellingson, B.M., P.Y. Wen, and T.F. Cloughesy, *Modified Criteria for Radiographic Response Assessment in Glioblastoma Clinical Trials.* Neurotherapeutics : the journal of the American Society for Experimental NeuroTherapeutics, 2017. **14**(2): p. 307-320.
57. Schepkin, V.D., et al., *Initial in vivo rodent sodium and proton MR imaging at 21.1 T.* Magnetic resonance imaging, 2010. **28**(3): p. 400-407.
58. Jacobs, M.A., T.S. Ibrahim, and R. Ouwerkerk, *AAPM/RSNA physics tutorials for residents: MR imaging: brief overview and emerging applications.* Radiographics, 2007. **27**(4): p. 1213-29.
59. Pooley, R.A., *AAPM/RSNA physics tutorial for residents: fundamental physics of MR imaging.* Radiographics, 2005. **25**(4): p. 1087-99.
60. Nishimura, D.G., *Principles of Magnetic Resonance Imaging*. 2010, Stanford University. p. 238.
61. Brown, R.W., Cheng, Y. C., Haacke, E. M., Thompson, M. R., Venkatesan, R., *Magnetization, Relaxation, and the Bloch Equation*, in *Magnetic Resonance Imaging*. 2014. p. 53-66.
62. McRobbie, D.W., et al., *MRI from Picture to Proton*. 2 ed. 2006, Cambridge: Cambridge University Press.
63. Chen, J., G.M. Lanza, and S.A. Wickline, *Quantitative magnetic resonance fluorine imaging: today and tomorrow.* Wiley interdisciplinary reviews. Nanomedicine and nanobiotechnology, 2010. **2**(4): p. 431-440.
64. Gruber, B., et al., *RF coils: A practical guide for nonphysicists.* Journal of magnetic resonance imaging : JMRI, 2018. **48**(3): p. 590-604.
65. Axel, L., Costantini, J., Listerud, J., *Intensity correction in surface-coil MR imaging.* Am J Roentgenol, 1987(148).
66. Winter, P.M. and N. Bansal, *TmDOTP(5-) as a (23)Na shift reagent for the subcutaneously implanted 9L gliosarcoma in rats.* Magn Reson Med, 2001. **45**(3): p. 436-42.
67. Huhn, K., et al., *Potential of Sodium MRI as a Biomarker for Neurodegeneration and Neuroinflammation in Multiple Sclerosis.* Frontiers in neurology, 2019. **10**: p. 84-84.
68. Ouwerkerk, R., et al., *Tissue sodium concentration in human brain tumors as measured with 23Na MR imaging.* Radiology, 2003. **227**(2): p. 529-37.
69. Nagel, A.M., et al., *3 Tesla sodium inversion recovery magnetic resonance imaging allows for improved visualization of intracellular sodium content changes in muscular channelopathies.* Invest Radiol, 2011. **46**(12): p. 759-66.
70. Lu, A., et al., *Quantitative sodium imaging with a flexible twisted projection pulse sequence.* Magnetic resonance in medicine, 2010. **63**(6): p. 1583-1593.
71. Boada, F.E., et al., *Fast three dimensional sodium imaging.* Magn Reson Med, 1997. **37**(5): p. 706-15.

72. Nagel, A.M., et al., *Sodium MRI using a density-adapted 3D radial acquisition technique*. Magn Reson Med, 2009. **62**(6): p. 1565-73.
73. Schepkin, V.D., et al., *Sodium magnetic resonance imaging of chemotherapeutic response in a rat glioma*. Magnetic resonance in medicine, 2005. **53**(1): p. 85-92.

Chapter 2

2 Materials and methodology

2.1 RF Hardware

To facilitate co-registered proton and sodium imaging, two separate radiofrequency (RF) coils were utilized: a proton birdcage RF coil and a curved sodium surface coil. The RF coils were designed such that the curvature of the sodium surface coil could fit snugly within the bore of the larger cylindrical proton birdcage coil. This would allow for co-registered images to be acquired and for the coils to be moved relative to each other.

Proton imaging was conducted using a custom-built 8-rung birdcage coil and RF shield. The dimensions of the cylindrical acrylic tube for the coil was 88.9mm in outer diameter (OD) with a form thickness of 3.2mm and 264mm in length. This tube had two outer nylon rings used to locate an RF shield concentrically about the RF coil. The dimensions of the shield were 356mm long with an 165mm OD. The loaded resonant frequency of this coil was tuned to 127.74MHz, the Larmor frequency of water protons at 3T. The Q factor for the birdcage coil was 200 [1]. The sodium images were obtained using a custom-built rectangular butterfly surface RF coil constructed on a cylindrical former with a diameter of 55.65mm. The dimensions of each surface coil were 47.86mm by 78.92mm and the coils were overlapped by approximately 15.66mm. Both channels on the coil were tuned to 33.8MHz while loaded with a 1% agarose phantom with a sodium concentration of 50mM filling the entire coil imaging volume. Figure 2-1 shows the image of the sodium coiled used.

Figure 2-1. Sodium surface coil shown from (L) a top-down view and (R) down the vertical axis with a cylindrical 50mM 1% agarose phantom placed in the coil.

2.2 Imaging phantoms

Custom imaging phantoms were constructed to evaluate the performance of the sodium RF hardware, imaging sequence, and intensity correction pipeline. Cylindrical 1% agarose phantoms were produced that matched the curved form of the surface coil. This method allowed for the phantom to completely mold to the shape of the coil and fill the entire imaging region. The phantoms were chosen to have a sodium concentration of 50mM, based on average physiological sodium concentrations [2].

2.3 DA3DPR protocol optimization for sodium MRI

Sequence evaluation and imaging was performed on a GE Discovery MR 750 3.0T MRI (General Electric Healthcare, Milwaukee, WI, USA**)** [3]. The DA3DPR sequence was provided by Dr. Akbari as described in Nagel *et al.* [4]. Sodium imaging was evaluated with two coil configurations: imaging with sodium coil alone and imaging while the proton birdcage was placed around the sodium coil. Imaging was performed at 1mm and 3mm isotropic resolution for evaluation of the imaging SNR. Imaging at 1mm resolution was performed with the addition of an insertable gradient coil. Since excitation and encoding gradients were activated at the same time, greater accuracy is required, especially considering the radial encoding scheme which is more sensitive to imperfect gradients than Cartesian schemes [5]. Accuracy was hindered by eddy current issues which resulted in artifacts. Additionally, it was observed that 1mm voxels did not produce enough SNR to obtain measurable TSC in tissue in a reasonable amount of time. To achieve useful imaging SNR within a reasonable imaging session, it was evident that 1mm isotropic resolution would be challenging, and 3mm isotropic resolution was chosen for the *in vivo* measurements of tissue sodium concentration (TSC).

Imaging protocols at 3mm isotropic resolution were optimized with the addition of a “shift agent”, thulium-1,4,7,10-tetraazacyclododecane 1,4,7,10-tetrakis(methylene phosphonate) (Tm-DOTP^{5-}) to a sodium reference vial [6]. The purpose of doping a phantom with a shift reagent is to change the resonant frequency of the ^{23}Na nucleus in contact with the reagent. This “frequency-shifted” reference vial was used as a reference marker in a known and consistent location across longitudinal imaging sessions. This produced a well resolved second signal peak from the sodium inside the tube. This peak could be used to determine the amount of RF energy needed to excite the magnetization of the sodium nuclei through 90° at a repeatable position with respect to the RF coil. The sodium peak from the imaging subject itself could not be used as within the imaging space of the surface coil, increases in TG could alter the distribution of α within the space. This would be inconsistent between subjects and it would be difficult to reliably reproduce the same excitation profile across different imaging sessions. Data reported by Winter *et al.* was used to map the relationship between shift agent concentration and frequency shift for the sodium nucleus. In conjunction with tests using solutions of different concentrations, a shift of 1000Hz was achieved given the solubility limits of Tm-DOTP^{5-}. A solution of 200mM of Tm-DOTP^{5-} and 2M NaCl solution was used as a reference peak for setting transmit gain (TG) for the surface coil. By implementing the reference marker in a single repeatable location for all longitudinal imaging sessions, a consistent and replicable excitation profile can be achieved with a surface coil. The shift reagent reference tube (75.85mm length by 11.42mm diameter) was placed in a defined position at the center of the imaging region of the coil. The shifted peak was confirmed visually on the scanner and TG was determined from the maximum observed amplitude of the shifted peak. This reference tube was then removed prior to beginning sodium image acquisition.

2.4 Cell culture

C6 rat glioma cells (CCL-107, American Type Culture Collection, Manassas, VA, USA) were cultured in Dulbecco's Modified Eagle Media (DMEM) (Wisent, Montreal, QC, CA) containing 10% fetal bovine serum (FBS), 1% antibiotic-antimycotic and supplemented with 4-times concentration of non-essential amino acids and 2% L-glutamine. Cells were grown at 37°C in 5% CO_2. Cells were evaluated for mycoplasma using the MycoAlert Mycoplasma Detection Kit (Lonza, Basel, Switzerland).

2.5 Animal model

An orthotopic glioma model was used for this study. On day 0, 200-250g male Wistar rats (Charles River Laboratories, Wilmington, MA, USA) underwent stereotactic surgery for cell implantation into the brain. Fur on the superior side of the rat head was removed and a midline incision was made. Fascia was pushed aside to expose the skull surface and bregma and lambda were landmarked and horizontally leveled. A 2.5mm burr hole was drilled 1mm posterior and 3mm right-lateral to bregma. A 25G Hamilton microliter syringe (Hamilton 700 series) was advanced to a 4mm depth and used to inject 10^6 C6 glioma suspended in 10μL of phosphate buffered solution (PBS) at a rate of 3μL/min. The needle was left in place for 1 minute before extraction. The surgical site was flushed with a sterile saline solution to wash away any cells which may have effused from the injection site through the burr hole. Finally, bone wax was used to fill the burr hole to block any additional cells from effusing. Animals were imaged on days 7, 10, 12 and imaged every 3rd day after that except for rat 1. This animal received imaging on days 7, 10, and then every 2nd day after that. When tumours reached a volume of greater than $150mm^3$, animals were designated to: first a control group which received no therapy (n=4) and followed by a treatment group (n=3). The treatment group received 40mg/kg of Temozolomide (TMZ, Sigma Aldrich, Miamisburg OH, USA) dissolved in dimethyl sulfoxide (DMSO, Sigma Aldrich, Miamisburg OH, USA) via intra-peritoneal injection for 5 consecutive days. At endpoint, animals were perfused, and tissue was collected for histological examination. All animal procedures were conducted in accordance with relevant guidelines by the University Council on Animal Care and the Animal Use Subcommittee (AUP 2018-164).

2.6 In vivo imaging

2.6.1 Sodium imaging

Animals first underwent imaging with the sodium surface RF coil which allowed for easier animal placement and adjustment. This was followed by subsequent imaging with the proton birdcage RF coil. The sodium coil was positioned on an MR compatible tray comprised of a curved cylindrical acrylic former suspended from plastic rails. This configuration placed the animal head near the isocentre of the MRI bore as well as allowed for the placement of a proton birdcage RF coil and shield around the animal without any additional repositioning of the animal (Figure 2-2). Solutions with sodium concentrations of 30mM, 50mM, 70mM, and 100mM in 2mL reagent bottles were placed along the underside of the coil. These reference vials were used for the correction of the RF coils sensitivity profile and to determine absolute TSC.

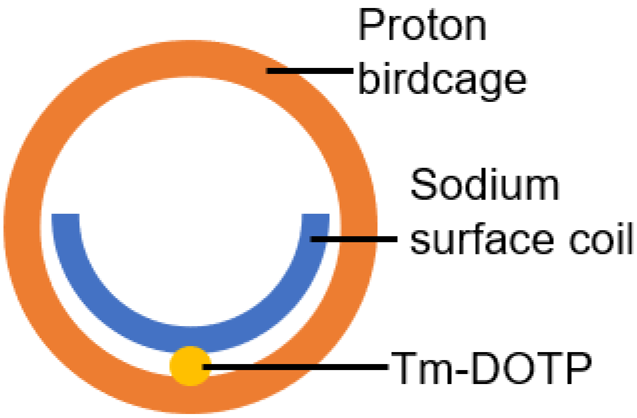

Figure 2-2. An illustrative schematic showing the positioning of the proton birdcage, sodium surface coil and animal position down the vertical axis. The proton birdcage is attached to external rails which allow it to move independently from the sodium surface coil.

All animal imaging was conducted on a GE Discovery MR 750 3.0T MRI (General Electric Healthcare, Milwaukee, WI, USA). A detailed image showing the imaging setup is shown in Figure 2-3. Sodium imaging was conducted using a density-adapted 3-dimensional projection reconstruction sequence (DA3DPR) (TE=0.5ms, TR=100ms, T_{aq}=8ms, flip angle (α)=90°, FOV=80mm isotropic, NEX=10, imaging time=12mins) [1]. The transmit gain for imaging was set based on a vial of 200mM Dm-DOTP^{5-} and 2M sodium chloride solution placed in the center of the coil's imaging area. This solution produced a sodium signal peak with a shifted frequency of approximately 1000Hz [2]. Images were reconstructed using a custom MATLAB script (MathWorks, Natick, MA, USA) to an imaging matrix size of 27 × 27 × 512 with 3mm isotropic imaging voxels.

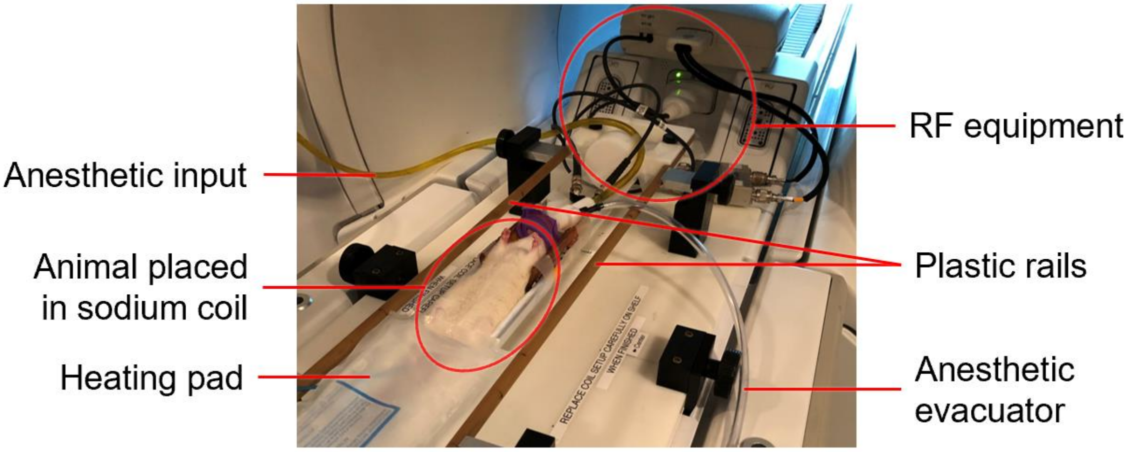

Figure 2-3. A photograph showing a typical set up for sodium imaging. The sodium coil and animal in supine position are placed on a specially constructed tray which suspends an acrylic half-pipe between the rails. Anesthesia and heating can be placed around the animal. The halfpipe is slid through the bore of the proton coil which is centered by nylon end-rings to position it along the rails. This allows the proton coil to be positioned central to the animal and sodium coil.

2.6.2 Proton imaging

To acquire proton images, the proton birdcage coil and shield were slid onto the rails and positioned to be concentric with and centred on the sodium coil. For each imaging session 3D T_2-weighted images and 3D pre- and post- gadolinium-DTPA (0.5mmol/kg; Magnevist, Bayer, Leverkusen, Germany) contrast enhanced (CE) T_1-weighted images were acquired. The T_2-weighted images were obtained using a 3D fast spin echo sequence (FSE) (CUBE, General Electric Healthcare, Milwaukee, WI, USA) with the following parameters: FOV=60mm isotropic, acquisition matrix=128×128, slice thickness=0.5mm, bandwidth=62.50MHz, NEX=3, TR=2432ms, TE=60ms, echo train length (ETL)=120, imaging time=12 minutes. The T_1-weighted images were also obtained using a general 3D FSE sequence with the following parameters: FOV=60mm isotropic, acquisition matrix=128 × 128, slice thickness=0.5mm, bandwidth=31.25MHz, NEX=1, TR=281ms, TE=18.2ms, ETL=10, imaging time=10 minutes. Post-CE images were acquired 30s after Magnevist (Bayer, Leverkusen, Germany) injection.

2.7 Image processing

2.7.1 Intensity correction and quantification

Sodium images were reconstructed using MATLAB (MathWorks, Natick. MA, USA), GE Orchestra (General Electric Healthcare, Milwaukee, WI, USA) and the Michigan Image Reconstruction Toolbox (Jeffery A. Fessler, “Michigan Reconstruction Toolbox”, web.eecs.umich.edu/~fessler/code/). Sodium images were reconstructed into an imaging matrix volume of 27 × 27 × 512 with 3mm isotropic imaging voxels. To prepare images for intensity correction, ITK-SNAP (www.itksnap.org, [7]) was used to perform region of interest (ROI) segmentations. The subject and sodium reference vials were segmented from the background noise using ITK-SNAP’s built-in semi-automatic segmentation tool. The mask generated from this segmentation was used with a custom MATLAB script (MathWorks, Natick. MA, USA) for purposes of correction of the non-uniform signal sensitivity profile of the sodium surface coil.

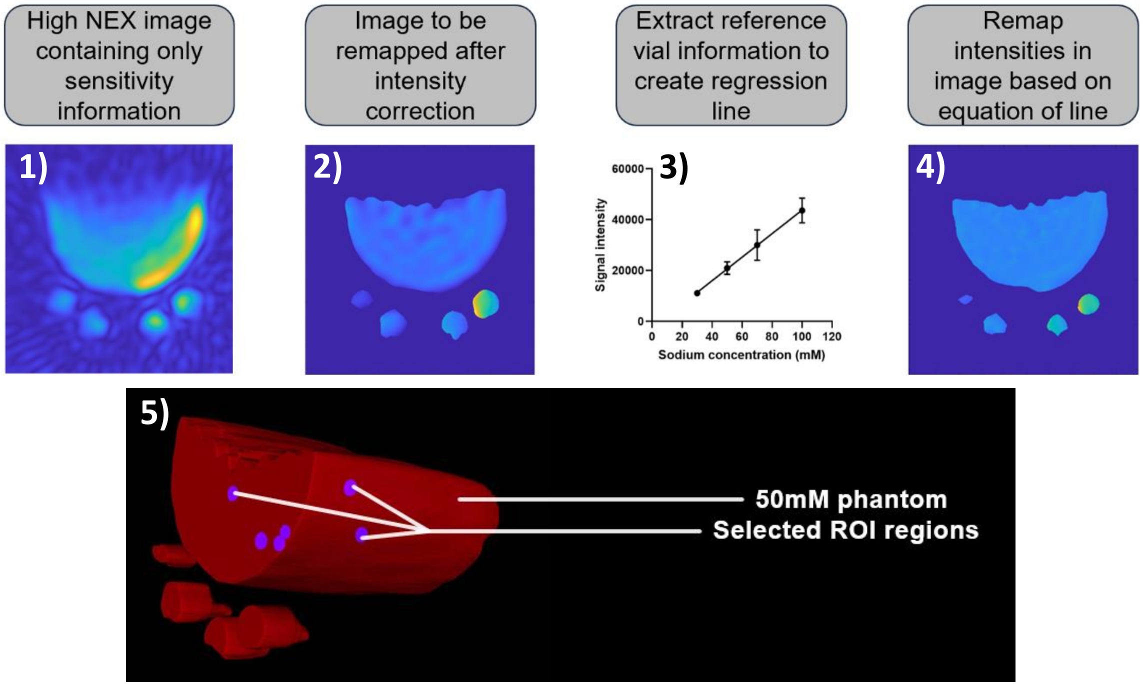

Figure 2-4. Schematic showing the major steps and outputs in intensity correction pipeline. **1)** An intensity normalized sensitivity axial image of a 50mM 1% agarose cylindrical phantom with four 50mM reference vials along the bottom. Acquired with 30 averages **2)** A segmented and intensity corrected image of a 50mM 1% agarose phantom with 30mM, 50mM, 70mM, and 100mM reference vials along the bottom. **3)** A linear regression formed through a plot of known sodium concentration in the segmented reference vials versus the average signal intensity in the segmented reference vials. The line is used to remap signal intensities in the image to their corresponding concentration. Error bars represent standard deviation of pixel measurements in each reference vial. **4)** Final image and reported average concentrations ± SD after intensity remapping showing the 50mM phantom and reference vials along the bottom. Measurements in small ROIs range from 47.9 ± 2.7mM to 51.5 ± 1.6mM. The average ± SD across all 6 sample ROIs was 49.5 ± 2.5mM. **5)** Showing the ROI selection (blue) within the volume of the phantom (red) rendered from segmentations take in ITK-SNAP.

To correct for intensity variation over the imaging area of the surface coil, a high SNR image containing only sodium intensity variation was obtained by using a 50mM 1% agarose phantom and 50mM reference vials. This sensitivity map was normalized to then obtain a normalized sensitivity map which could be used to scale intensities in an *in vivo* image. To process an *in vivo* image, a mask of the areas of interest (main area to be corrected and reference vials) was made using the semi-automatic segmentation tool in ITK-SNAP. This mask was eroded to address observable partial volume effects (PVE), especially in the edge regions of the reference vials. The average noise in the image was calculated from an averaged background ROI and then subtracted from each pixel to address the offset across the imaging volume which improves the precision of the quantification. Sensitivity correction was obtained by dividing the subject image by the normalized sensitivity map which adjusts pixel intensities to account for the signal fall off. Using the normalized sensitivity map, areas close to the surface of the coil are typically divided by larger numbers while areas further away from the surface of the coil would be divided by smaller numbers. This would offset the intensity fall of due to the surface coil.

To quantify sodium measurements from the intensity corrected image, first the average intensities from the known reference vials were extracted. These intensity values were mapped against their known concentrations to determine a line of best fit. This line was used to remap the pixel intensities across the rest of the image to concentration values. This pipeline was validated through the quantification of known 40mM and 80mM saline phantoms which were used to fill the imaging volume. This was followed by *in vivo* validation by evaluating healthy brain TSC in rats and comparing these values against known values from literature. Healthy rats (*n*=3) underwent a proton and sodium imaging session. Images were processed as described in section 2.6.2 and whole brain segmentations were obtained to determine the TSC of the healthy brain.

2.7.2 Image analysis

Manual registration of sodium and proton images was achieved using rigid linear transforms in 3D Slicer (www.slicer.org, [8]). Additionally, sodium images were resampled into the same voxel spacing as the proton images. Measurements for tumour volume from T_1- and T_2-weighted images were obtained from manual segmentations in ITK-SNAP (www.itksnap.org, [7]). Tumour boundaries from T_1-weighted images were determined based on post-CE images. T_2-weighted anatomical proton images were used as a guide to manually segment the tumorous regions to determine tumour TSC values from sodium images for each animal in the experiment.

As a comparison, matched baseline “contralateral” sodium measurements for each animal, a tumour free region in the posterior portion of the brain – far away from where the main tumour would grow was segmented out for measurement. Additional TSC measurements from healthy, tumour-free animals were obtained using the same registration methods. Whole brain segmentations were used to determine average healthy brain TSC.

2.8 Endpoint histology

At experimental endpoint, animals were euthanized and perfused with 4% paraformaldehyde (PFA) in PBS. The whole brain was then extracted and stored in 4% PFA at 4°C for 24 hours. After fixation, brains could be placed in PBS at 4°C for long term storage or prepared for cryo-sectioning.

For cryo-sectioning, brains were placed in solutions of increasing sucrose concentration (10%, 20%, 30%) until fully sunken to extract water content. After which the brain would be embedded in optimal cutting temperature (OCT) medium and frozen on dry ice before moving to long term storage at -20°C. Ten-micron sections were obtained using a microtome-cryostat (Leica CM1860, Wetzlar, Germany) and stained for hematoxylin and eosin (H&E). Whole-mount sectioned slices were scanned using the EVOS imaging system (M7000, ThermoFisher Scientific, Waltham, MA, USA).

2.8 Statistics and analysis

Statistical analyses were performed using GraphPad Prism v8 (GraphPad Software Inc., California, USA). A two-way ANOVA and Tukey's *post hoc* was performed to investigate endpoint TSC. Exponential growth curve fitting was performed to model tumour growth based on tumour volume measurements over time. This relationship was then used to determine the tumour growth rates. Linear regressions were performed to identify any trends in the between measures and Pearson correlation analyses were performed to determine the strength of those trends.

2.9 References for Chapter 2

1. Lim, H., et al., *Construction and evaluation of a switch-tuned (13) C - (1) H birdcage radiofrequency coil for imaging the metabolism of hyperpolarized (13) C-enriched compounds.* J Magn Reson Imaging, 2014. **40**(5): p. 1082-90.
2. Christensen, J.D., et al., *Quantitative tissue sodium concentration mapping of normal rat brain.* Magn Reson Med, 1996. **36**(1): p. 83-9.
3. Foster-Gareau, P., et al., *Imaging single mammalian cells with a 1.5 T clinical MRI scanner.* Magn Reson Med, 2003. **49**(5): p. 968-71.
4. Nagel, A.M., et al., *Sodium MRI using a density-adapted 3D radial acquisition technique.* Magn Reson Med, 2009. **62**(6): p. 1565-73.
5. Moussavi, A. and S. Boretius, *Imperfect magnetic field gradients in radial k-space encoding-Quantification, correction, and parameter dependency.* Magn Reson Med, 2019. **81**(2): p. 962-975.
6. Winter, P.M. and N. Bansal, *TmDOTP(5-) as a (23)Na shift reagent for the subcutaneously implanted 9L gliosarcoma in rats.* Magn Reson Med, 2001. **45**(3): p. 436-42.
7. Yushkevich, P.A., et al., *User-guided 3D active contour segmentation of anatomical structures: Significantly improved efficiency and reliability.* NeuroImage, 2006. **31**(3): p. 1116-1128.
8. Fedorov, A., et al., *3D Slicer as an image computing platform for the Quantitative Imaging Network.* Magnetic resonance imaging, 2012. **30**(9): p. 1323-1341.

Chapter 3

3 Results and analysis

3.1 Results

To evaluate sequence performance and optimization, image quality from different DA3DPR acquisition protocols were evaluated. Comparisons between 1mm isotropic and 3mm isotropic imaging resolutions showed that overall SNR was higher using the insertable gradient system compared to the clinical gradient system. Qualitative observation indicated that sodium MR image quality at 3mm imaging resolution was higher than at 1mm imaging resolution, as expected. Sequence implementation using the insertable gradient system introduced new artefacts and challenges regarding feasibility as unwanted image artefacts such as blurring, and ringing were common. Additionally, hardware limitations were encountered due to the sensitivity of the radial sequence to eddy currents and gradient imperfections. As a result, *in vivo* imaging was acquired without the gradient insert system.

To optimize the addition of the shift reagent Tm-DOTP^{5-} for 3mm imaging resolution *in vivo* at clinical settings, a simulation of shift reagent concentration to reported frequency shift based on past literature was created. The final concentrations of ^{23}Na and TmDOTP^{5-} were determined by considering the amount of sodium for a well-defined peak and the solubility limits of TmDOTP^{5-} in water. Figure 3-1A shows the final observed peak which has been shifted approximately 1300 Hz from the main sodium peak. The combination of the DA3DPR sequence and the shift reagent was used to image a 50mM 1% agarose phantom. It was determined within the imaging area of the coil, an average

SNR of 14.9 could be achieved for images averaged 10 times (imaging time=12 minutes). A representative axial slice of a cylindrical phantom filling the imaging volume is shown in Figure 3-1B. It should be noted, an asymmetric signal profile was observed from the coil upon image reconstruction. This asymmetry was not observable from the bench and is likely to be the result of something further down the receive chain. This asymmetry did not affect analysis as the intensity correction pipeline was able to offset the profile.

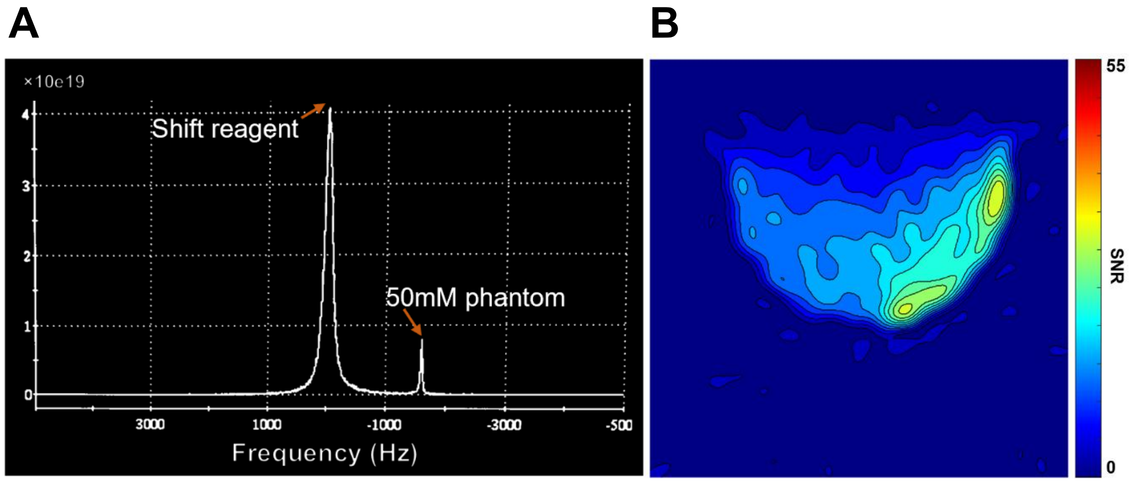

Figure 3-1. (A) ^{23}Na FID spectrum showing the (L) shift reagent signal and (R) signal from 50mM 1% agarose cylindrical phantom with frequency centered on shift reagent peak. **(B)** Representative axial slice of a cylindrical 50mM 1% agarose phantom showing SNR of coil in imaging region. Image was acquired with 10 averages over 12 minutes.

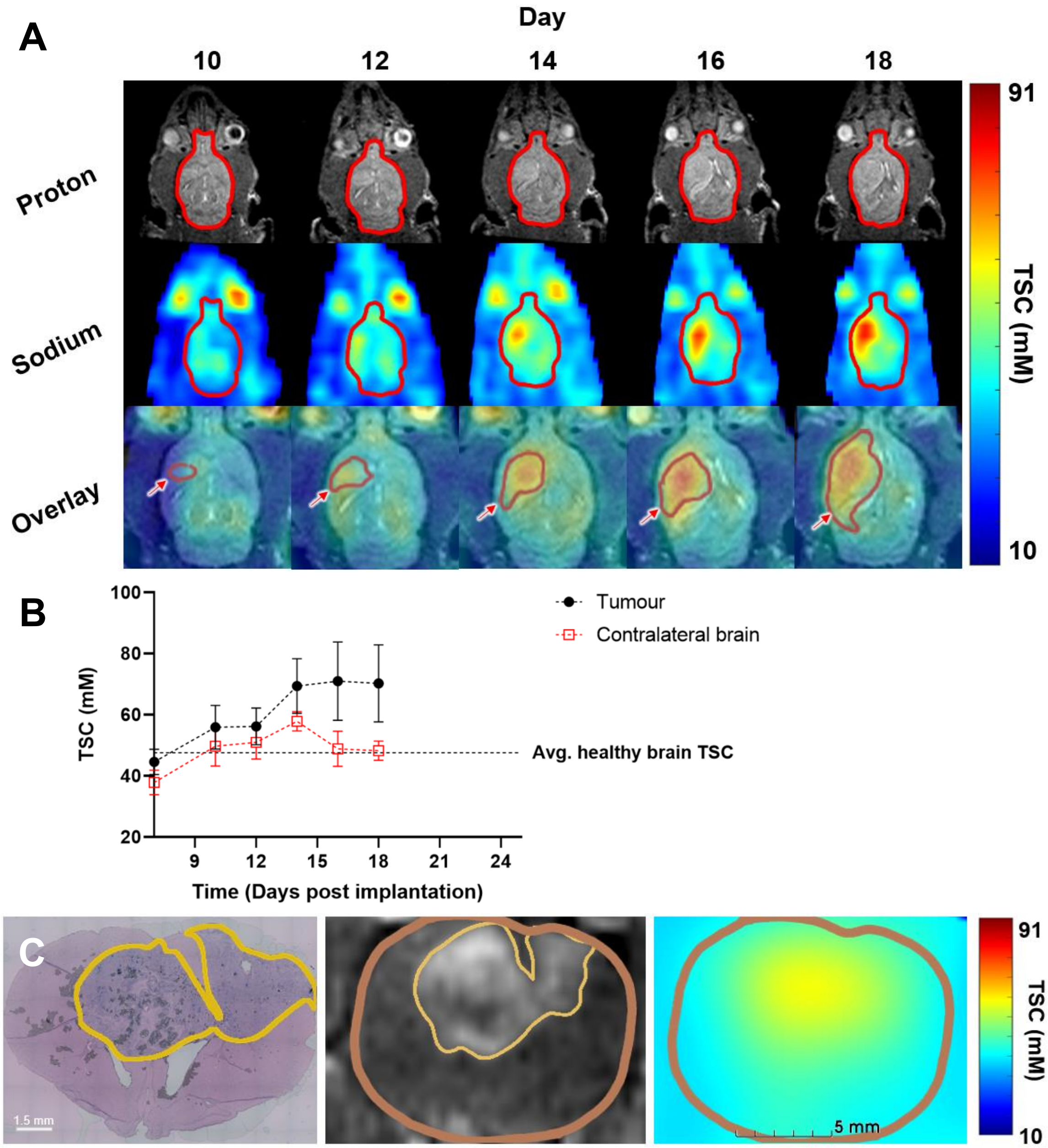

Figure 3-2. (A) Single representative animal from the non-treatment group. Bottom panel shows a zoomed in view of sodium images overlayed onto T_2-proton weighted images at longitudinal time points. Tumours are outlined by yellow boundaries. **(B)** Graph of average tissue sodium concentration ± SD for representative animal for both the tumorous region and contralateral brain region. (**C)** Side-by-side H&E histology, T_1-weighted image, and sodium image of non-treated animal at endpoint. Tumours are outlined in yellow and the brain in brown.

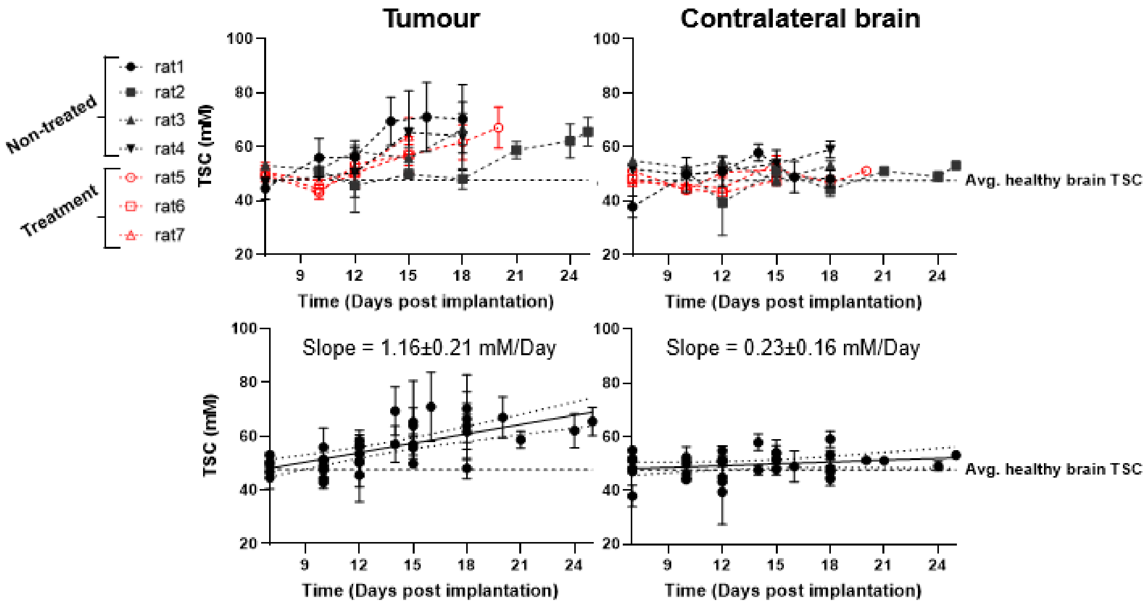

Figure 3-3. Graph of average tissue sodium concentration ± SD for (L) tumour and (R) contralateral tumour-free region for all imaging time points. Top row shows all animals and bottom row averages all cohorts to obtain a linear regression for all animals. Dotted lines show the 95% confidence interval. The slope for TSC versus time for the combined tumour group was significantly different from zero ($p<0.05$) and not significantly different from zero for the combined contralateral brain group ($p=0.15$). Slopes for the tumour region and the contralateral tumour-free region were significantly different ($p<0.05$).

A total of 7 rodents were monitored using longitudinal sodium imaging at multiple time points post-implantation. These animals were split into control (*n*=4) and treatment (*n*=3) groups. Figure 3-2A shows a representative animal’s sodium, proton and overlaid sodium and proton MR images while the animals’ representative TSC measurements over time are show in Figure 3-2B. A visible increase in the area and concentration of TSC localized to the tumour can be observed starting from day 12. T_1-weighted proton images and sodium images are also shown next to a corresponding H&E histology slide in Figure 3-2C. This shows the correspondence between the histological tumour area and what can be observed from the imaging data. The boundaries of the tumour are clearly visible and well defined in the T_1-weighted images, however the reduced resolution (3mm isotropic) in the sodium images show a lack of similar definition. Figure 3-3 shows the longitudinal changes in TSC across all animals in both control and treatment groups. Increasing TSC over time can be observed in the tumours while TSC in the contralateral brain stays relatively constant for both the control and treatment groups. The increase in TSC over time in the tumour has a slope significant from zero (slope = 1.16 ± 0.21mM/day, $p<0.0001$). The slope of TSC versus time in the contralateral brain regions is not significantly different from zero (slope = 0.23 ± 0.16mM/day, $p=0.15$).

Contrast enhanced T_1-weighted imaging was acquired for 5 animals out of the total 7. Animals in both treated ($n=3$) and non-treated ($n=2$) cohorts received CE MRI. Although T_1-weighted imaging is typically used in clinical imaging, our model saw the volume measurements from the T_2-weighted images better captured the bounds of the TSC distribution. Overall, there was more inhomogeneity in T_1-weighted images, which could be indicative of necrosis or changes in the permeability of the blood tumour barrier. Tumour morphology from T_2-weighted images were found to better correlate with tissue sodium distribution compared to T_1-weighted images, especially in control animals. This was qualitatively confirmed by visible inspection at endpoint by histology. The volume difference between the T_1-weighted and T_2-weighted measurements was on average 350.4 ± 123.18mm^3 for control animals at endpoint. An example of this discrepancy can be seen in Figure 3-4.

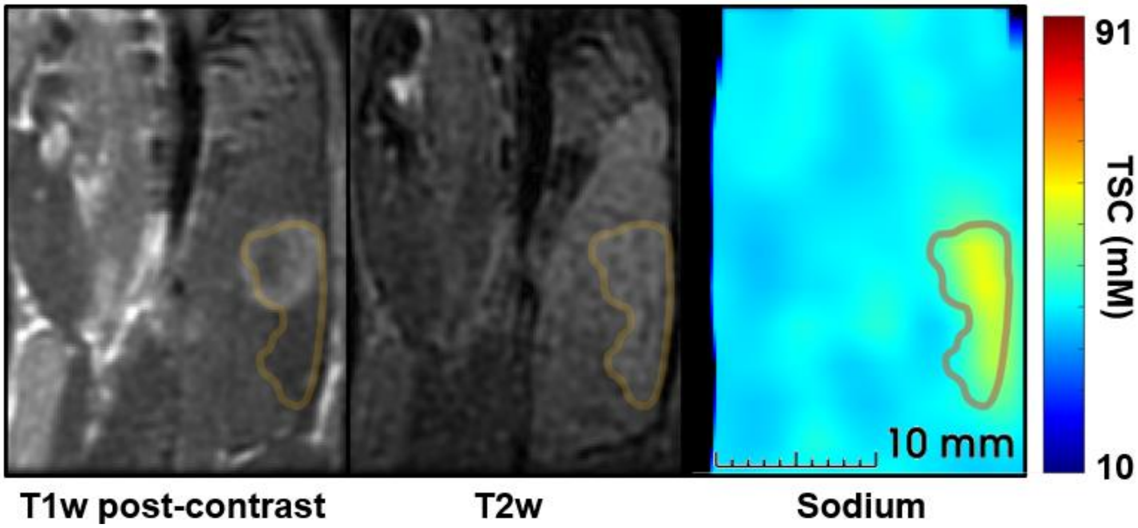

Figure 3-4. Representative animal showing a sagittal view of the brain (from left to right: T_1-weighted post-CE, T_2-weighted, sodium MRI images). Outline shows the boundaries of the tumour as taken from the T_2 volume also overlayed on the same position in the T_1-weighted post-CE and sodium images. Image resolution for the above images were 0.5mm^3, 0.5mm^3, and 3mm^3 respectively.

Figure 3-5 shows the tumour volumes extracted from the T_2-weighted proton images plotted against the average TSC measurements from the tumours for both groups. Average tumour TSC increased with volume for both non-treated and treated animals. However, the rate of this increase did not differ significantly between groups (p=0.42). A vertical line indicating a volume of 150mm^3 is included as that is the volume where reliable quantification of sodium signal localization to the tumour was possible. This represents approximately six sodium imaging voxels for our TSC imaging. Overall, average tumour volume at endpoint in the control group trended higher than in the treatment group, however this difference was not significant.

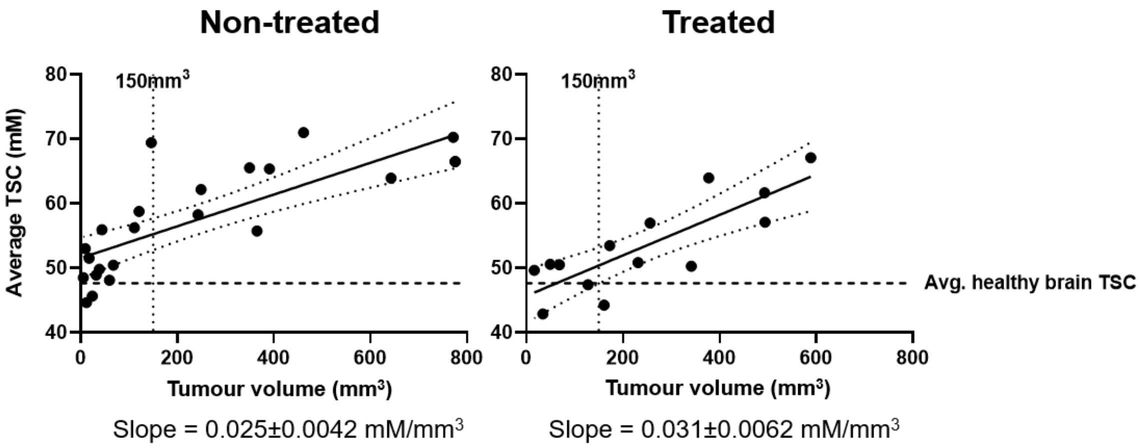

Figure 3-5 Graph of average tissue sodium concentration for (L) non-treated and (R) treated for measured tumour volumes. Dotted lines show the 95% confidence interval for the linear regression. Slopes of average TSC versus tumour volume were not significantly different at a 95% confidence level for non-treated versus treated groups (p=0.42).

Figure 3-6 shows tumour growth rate derived from volume measurements plotted against average TSC. A positive correlation between growth rate and average tumour TSC for both control (r=0.78) and treatment cohorts (r=0.67) was observed. The slope for this relationship did not differ significantly between groups (p=0.57). The range of growth rates observed in the control group is larger than the range of growth rates observed in the treatment group. The maximum growth rate in the control group is 265.8±0.1mm^3/day while the maximum in the treatment group is 136.2±0.2mm^3/day. This error was obtained from the 95% confidence interval. The uncertainty in the difference of these two rates is 129.6±0.3mm^3/day. As this difference is represents greater than 4 standard deviations, the difference between the growth rates are significant.

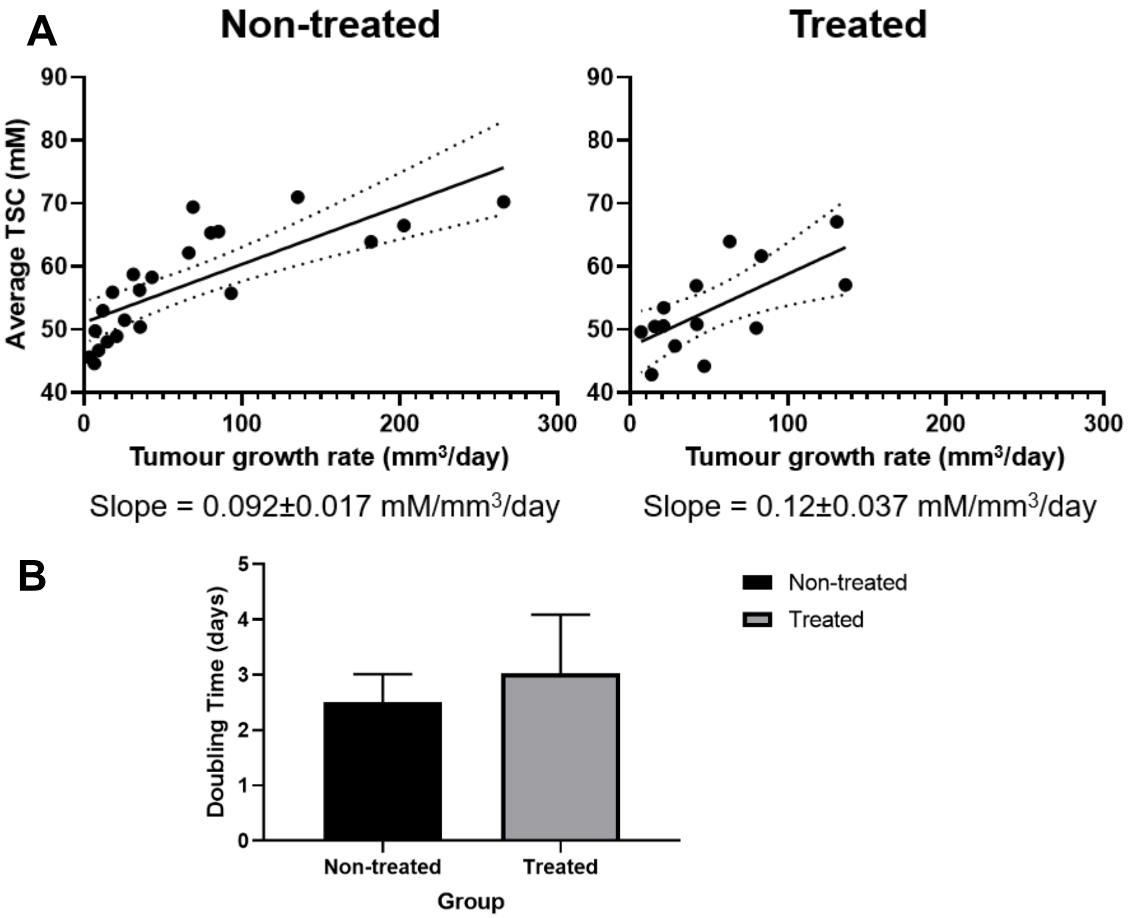

Figure 3-6. (A) Graph of average tissue sodium concentration in tumours for (L) non-treated and (R) treatment cohorts for tumour growth rate. Dotted lines show the 95% confidence interval for the linear regression. Slopes not significantly different at a 95% confidence level (p=0.57). **(B)** Graph of average doubling time of tumour volumes for the non-treated and treated animal groups. Differences in doubling times were not significant (p=0.23).

The relationship between time after injection and ΔTSC between the tumour and contralateral brain showed that differences between brain region did not significantly differ depending on cohort and overall trended in a positive direction. It was observed that overall differences in TSC between the tumour region and contralateral brain increased. Lastly, a comparison of TSC at endpoint across treatment groups and brain regions showed that differences were significantly different only between regions (p<0.001) and not between cohorts.

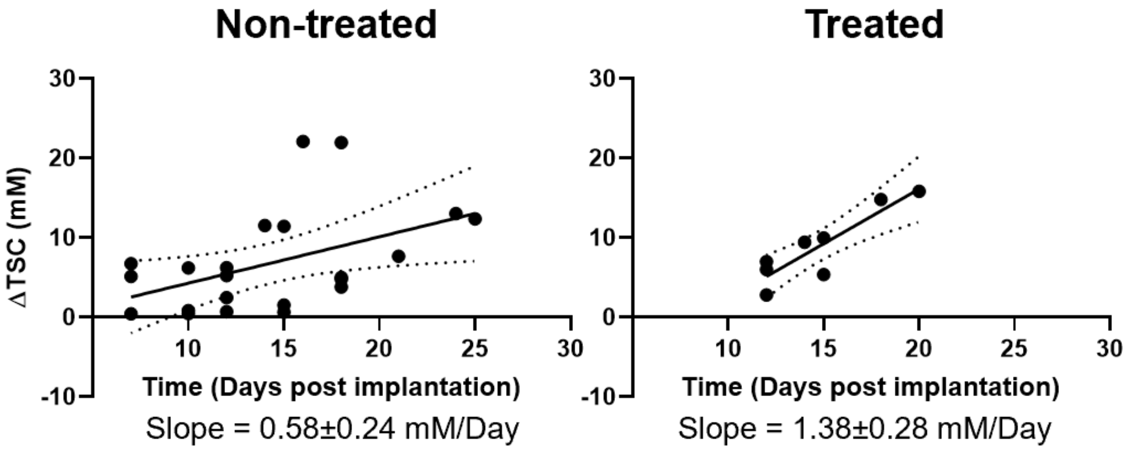

Figure 3-7. Graph of ΔTSC between tumorous region and contralateral brain for time matched points for (L) untreated and (R) treatment cohorts. Dotted lines show the 95% confidence interval for the linear regression. Slopes are not significantly different at a 95% confidence level (p=0.18).

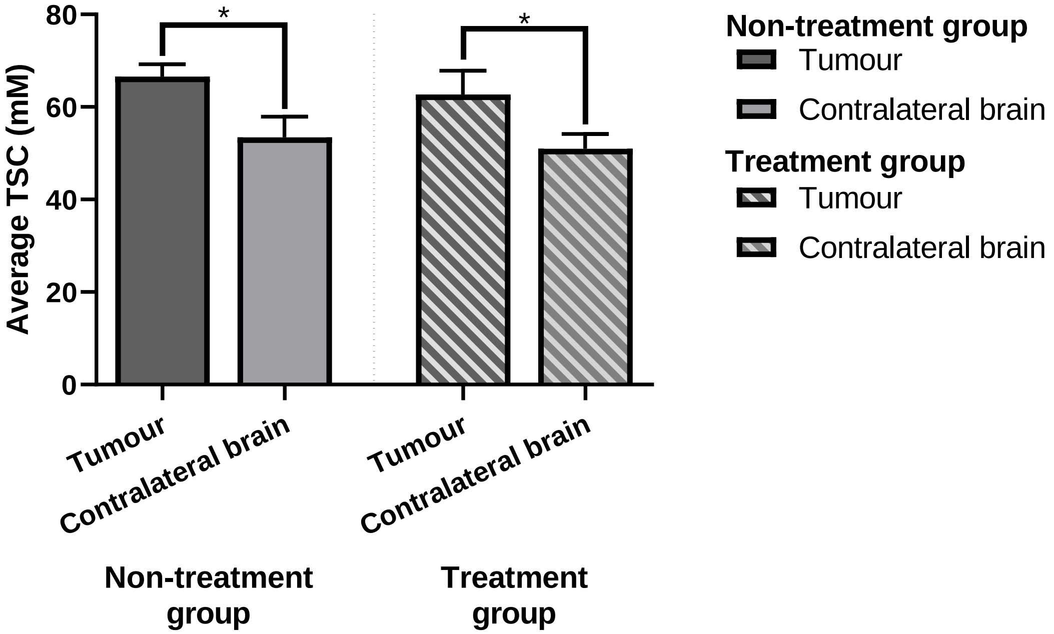

Figure 3-8. Graph of average TSC ± SD at endpoint for the tumorous region and contralateral brain region. Differences between brain region are significant for both non-treatment and treatment groups ($p<0.0001$). Average tumour TSC ($p=0.59$) and average contralateral brain TSC ($p=0.84$) at endpoint were not significantly different between treatment and non-treatment groups.

3.2 Discussion

In this study we demonstrated the first implementation of DA3DPR sodium imaging to study an orthotopic glioblastoma tumour model in rats at 3T. The sequence was successfully implemented at 3T using the clinical gradient. In addition, sodium images from the surface coil imaging was successfully quantified using our inhouse algorithm. The implementation of this sequence with the addition of a proton birdcage which slid over the sodium setup meant that anatomical images could be intrinsically co-registered with sodium images. Our preliminary study showed that the imaging protocol was sensitive to changes in TSC over time and in different brain regions. In the clinic, CE T_1-weighted imaging and T_2-weighted imaging are typically used to assess glioma. A combination of T_1-weighted and T_2-weighted proton anatomical images with sodium MRI images allowed for the investigation of the relationship between TSC and the physical characteristics of the tumours, such as volume and growth rate. Sodium MRI could additionally add molecular information about glioma for this preclinical model.

The segmentation based on the anatomical images allowed for the extraction of tumour volumes and TSC. Based on tumour volume measurements and observable signal localization, sodium signal can be reliably quantified for tumour volumes larger than 150mm^3. Tumour volume was a limiting factor in sodium quantification due to the voxel size in the sodium scans, thus diffuse areas of the tumour or offshoots of the main mass which can be visualized in the proton scans cannot be detected in the sodium. Voxel size will likely continue to be a limiting factor in sodium MRI studies as most studies report an isotropic resolution of around 2.5mm^3 in both preclinical and clinical settings [1-4]. It should be noted that imaging in these studies tended to have a greater number of averages and therefore longer imaging durations. The analysis showed that TSC increased over time within the tumours as they grew. Increases in tumour growth rate were additionally correlated with increasing TSC. Ultimately this indicates that the sodium imaging protocol is supported by anatomical imaging as TSC was extracted based on the observable tumour from T_2-weighted images. Based on the co-registration and segmentation, changes in the TSC could be observed specific to the tumour. This analysis revealed that this sodium imaging method and animal model did not show differences in the tumour TSC between control and treatment group animals. A few studies have investigated long-term trends in pre-clinical models using sodium MRI and clinically relevant proton sequences, thus the insights provided by this study provide valuable insight into possible trends and considerations for further studies of this type [5].

An evaluation of growth rate determined from the longitudinal segmentations showed there was an increase in tumour volume doubling time observed for animals in the treatment cohort. This difference is not significant therefore it is difficult to say whether treatment influenced the rate of growth of the tumours. This could explain the similarities in the TSC values for both cohorts. It should be noted that the range of growth rates was greater for control animals than the range of growth rates for treatment animals, which may indicate treatment influenced tumour growth which was not reflected in the TSC. This could partly be owed to the differing durations of survival between cohorts. The chemotherapy regiment was aggressive and animals in the treatment cohort deteriorated rapidly compared to animals in the control cohort. As a result, overall survival times for the treatment cohort were shorter. Ultimately it is unclear if the lack of differences were due to limitations with the imaging protocol itself, or limitations of the animal model.

A key measurement evaluated was the time matched difference between TSC in the tumour and TSC in the contralateral brain (ΔTSC). These differences increased over time as we observed increases in the tumour TSC compared to the relative steadiness in the contralateral brain TSC. It is important to recognize that the contralateral brain is not a perfect measurement of baseline TSC to evaluate changes against. As it is in the same organ as the tumour, this region is not healthy and is affected by the extracellular tumour environment. Inflammation, infiltration, and extracellular environment changes are potential factors that could affect the contralateral side [6]. These changes, in particular inflammation would result in TSC increases which may explain the observed upwards trend [7]. It is also likely that the chemotherapy had some effect on the cells in the contralateral brain. TMZ is not a targeted therapy and specifically functions via DNA alkylation, therefore all dividing cells in the body would be affected to some degree and cell death is likely to increase in the healthy dividing glial cells in the brain [8]. Therefore, the slight increase in TSC over time observed in the contralateral brain may point towards a combination of these described factors. We are interested in the contralateral region despite these limitations as it is within the same organ as the tumour and can therefore present the most relevant point for comparison.

We incidentally observed that regions of high TSC better correlated with tumour boundaries observed in T_2-weighted images rather than T_1-weighted images. This is of particular interest as evaluating changes on T_1-weighted images is the current clinical standard for evaluating treatment response. More recent guidelines for evaluating treatment response such as the Response Assessment in Neuro-Oncology (RANO) evaluate T_2-weighted images in addition T_1-weighted images, however this guideline is still mostly used for clinical trial purposes [9]. This indicates that sodium images provide information beyond that of T_1-weighted proton imaging, and that T_2-weighted contrast may be more specific to tumour size.

While our limited imaging was ultimately not able to discern between treatment and control groups, it is important to take into considerations the limitations and factors which impact this conclusion. Optimizing the model to be more sensitive to treatment could provide a way to better interrogate treatment effects on TSC changes. As mentioned previously, animals which received treatment experienced a more rapid decline due to the burden of chemotherapy in addition to the disease burden. This affected their overall survival and it is possible that animals were sacrificed before sodium changes could appear. Changing the timeline and method(s) of treatment for the animal model could potentially improve on this study. In a previous study by our group the same animal model was evaluated using magnetic resonance spectroscopic imaging of the metabolism of hyperpolarized [1-^{13}C] pyruvate. Animals were placed into one of 4 groups receiving: no treatment, chemotherapy by TMZ, radiotherapy, and concurrent chemo-radiotherapy. It was observed that animals which received the concomitant chemo-radiotherapy had longer survival compared to administering each therapy individually or no therapy at all [10]. This indicates that treatment influences survival and this effect can be modulated by the choice of which treatment to prescribe. By extending the timeline and lessening the burden of treatment, animals in the treatment cohort could survive for a greater length of time, which could allow any effects due to treatment to be more clearly observable. A similar study conducted at 9.4T evaluated animals over a much longer timeline after treatment [11]. In this study 10,000 9L cells were implanted in Fischer rats. These cells were permitted to grow for 17 days prior to a single treatment session with carmustine (BCNU). Animals were monitored for up to 30 days after treatment began. Through this extended timeline, an increase in TSC was observed until 5 days after treatment before a decrease was observed. Our results show a similar initial trend with increasing TSC however we ultimately were not able to follow the animals for an extended period after treatment. Given the shorter treatment duration compared to our study, it would be expected these animals received less therapeutic burden and that contributed to there improved survival.

The Warburg effect describes the altered cellular metabolism found in cancer cells. The major characteristic of this altered metabolism is the increase in glycolytic activity even in the presence of oxygen. This activity decreases the pH in the tumour microenvironment due to an increase in proton concentration. The electro-chemical exchange that occurs to rebalance the cell pH increases the local TSC inside the cancer cells [12-14]. This will reflect in changes in the intracellular and extracellular environment as the cells work to maintain electrochemical homeostasis. Ultimately our DA3DPR imaging is only sensitive to total TSC and not to specific sodium compartments. This dependence on the intracellular and extracellular compartment means that the observed TSC can be affected by any changes that may occur in these spaces such as changes in the extracellular sodium concentration and the relative volumes of these two compartments [7].

It is also important to recognize the impact of PVE on this study. Due to the large voxel size and reliance on segmentations based on anatomical proton images to obtain tumour TSC measurements, there are important considerations regarding the impact of PVE. Primarily, there is a consideration for the range and error associated with TSC. Many segmented voxels may contain sodium measurements from areas both inside and outside of the tumour. This ultimately impacts the accuracy and measurement uncertainty associated with the sodium observations. This challenge is likely to persist in applications involving sodium MR due to current the inherent spatial resolution associated with using spherical *k*-space trajectories and the rapid signal relaxation [15].

Sodium MRI has applications as a clinical molecular imaging modality due to its comparative ease of implementation compared to other molecular imaging techniques. Currently most of the research into preclinical sodium MRI occurs at high field strengths [11, 16]. While high field MR research has limited applicability to clinical translation, studies at lower fields have been conducted on humans [3, 4, 17]. These studies tend to focus on evaluating if TSC differences can be quantified for different disease states such as multiple sclerosis, hypertension, and diabetes [18-20]. Experimental work for interrogating specific applications and biomolecular relationships will still rely on preclinical imaging.

In conclusion, this study has successfully implemented a quantifiable DA3DPR imaging protocol for orthotopic C6 rat glioma and was able to characterize changes in the tumour TSC over time and between brain regions. Relationships between tumour growth rate and TSC was observed as well as better characterization of the relationship between sodium signal and tumour morphology based on T_1- and T_2-weighted images. As this study is a preliminary study, we saw no differences between the treated and non-treated groups. Future work for this study will include improving the animal model to allow for a longer experimental timeline as well as expanding the size of the groups for increased statistical power. This will likely provide a greater period for any changes due to treatment to manifest and improve overall survival in the cohorts. As mentioned previously, our research group has previously studied this model with animal cohorts which also underwent radiotherapy and concurrent chemo-radiotherapy. Including these treatment cohorts in a future sodium MR study would improve our understanding of how TSC can be affected by different treatment methods. This could also provide insight into more clinically relevant treatment responses as the standard of care for GBM includes concurrent chemo-radiotherapy. Lastly, the ability to move birdcage coils independent of the sodium coils introduces the opportunity to study the relationship sodium and proton imaging may have with other molecular MR markers such as hyperpolarized ^{13}C-labelled metabolites. This would provide additional molecular imaging metrics to observe the relationship between metabolism and TSC.

3.3 References for Chapter 3

1. Christensen, J.D., et al., *Quantitative tissue sodium concentration mapping of normal rat brain.* Magn Reson Med, 1996. **36**(1): p. 83-9.
2. Thulborn, K.R., et al., *Quantitative tissue sodium concentration mapping of the growth of focal cerebral tumors with sodium magnetic resonance imaging.* Magn Reson Med, 1999. **41**(2): p. 351-9.
3. Nunes Neto, L.P., et al., *Quantitative sodium imaging and gliomas: a feasibility study.* Neuroradiology, 2018. **60**(8): p. 795-802.
4. Ouwerkerk, R., et al., *Tissue sodium concentration in human brain tumors as measured with 23Na MR imaging.* Radiology, 2003. **227**(2): p. 529-37.
5. Schepkin, V.D., et al., *Proton and sodium MRI assessment of emerging tumor chemotherapeutic resistance.* NMR in biomedicine, 2006. **19**(8): p. 1035-1042.
6. Chistiakov, D.A. and V.P. Chekhonin, *Extracellular vesicles shed by glioma cells: pathogenic role and clinical value.* Tumour Biol, 2014. **35**(9): p. 8425-38.
7. Olde Engberink, R.H.G., V. Selvarajah, and L. Vogt, *Clinical impact of tissue sodium storage.* Pediatric Nephrology, 2020. **35**(8): p. 1373-1380.
8. Zhang, J., M.F. Stevens, and T.D. Bradshaw, *Temozolomide: mechanisms of action, repair and resistance.* Curr Mol Pharmacol, 2012. **5**(1): p. 102-14.
9. Chinot, O.L., et al., *Response assessment criteria for glioblastoma: practical adaptation and implementation in clinical trials of antiangiogenic therapy.* Current neurology and neuroscience reports, 2013. **13**(5): p. 347-347.
10. Lim, H., et al., *Monitoring Early Changes in Tumor Metabolism in Response to Therapy Using Hyperpolarized (13)C MRSI in a Preclinical Model of Glioma.* Tomography (Ann Arbor, Mich.), 2020. **6**(3): p. 290-300.
11. Schepkin, V.D., et al., *Sodium magnetic resonance imaging of chemotherapeutic response in a rat glioma.* Magnetic resonance in medicine, 2005. **53**(1): p. 85-92.
12. Kim, J.W. and C.V. Dang, *Cancer's molecular sweet tooth and the Warburg effect.* Cancer Res, 2006. **66**(18): p. 8927-30.
13. Warburg, O., F. Wind, and E. Negelein, *The metabolism of tumors in the body* J Gen Physiol, 1927. **8**(6): p. 519-530.
14. Stock, C. and S.F. Pedersen, *Roles of pH and the Na(+)/H(+) exchanger NHE1 in cancer: From cell biology and animal models to an emerging translational perspective?* Semin Cancer Biol, 2017. **43**: p. 5-16.
15. Mentrup, D. and H. Eggers, *Signal Decay Correction in 2D Ultra-Short Echo Time Imaging.* Magnetic Resonance Materials in Physics, Biology and Medicine, 2006. **19**(2): p. 62-70.
16. Schepkin, V.D., et al., *Initial in vivo rodent sodium and proton MR imaging at 21.1 T.* Magnetic resonance imaging, 2010. **28**(3): p. 400-407.
17. Nagel, A.M., et al., *Sodium MRI using a density-adapted 3D radial acquisition technique.* Magn Reson Med, 2009. **62**(6): p. 1565-73.
18. Kopp, C., et al., *23Na magnetic resonance imaging-determined tissue sodium in healthy subjects and hypertensive patients.* Hypertension, 2013. **61**(3): p. 635-40.
19. Huhn, K., et al., *Potential of Sodium MRI as a Biomarker for Neurodegeneration and Neuroinflammation in Multiple Sclerosis.* Frontiers in neurology, 2019. **10**: p. 84-84.

20. Kannenkeril, D., et al., *Tissue sodium content in patients with type 2 diabetes mellitus.* J Diabetes Complications, 2019. **33**(7): p. 485-489.

Chapter 4

4 Overview

This thesis highlights the opportunities and challenges associated with the use of sodium MRI for assessment of pre-clinical tumours. An imaging protocol was optimized for a pilot investigation of changes in sodium in a preclinical treatment model of glioblastoma. Sodium levels were demonstrated to be sensitive to tumour growth in a C6 GBM rat model. However, the model itself presented challenges when investigating the differences in TSC when treatment is applied. The main scientific contributions of this work will be summarized below.

4.1 Summary and conclusions

For this thesis, a new imaging sequence for sodium was introduced to our facilities and optimized for *in vivo* imaging using a surface coil. This protocol was then applied to investigate the use of sodium MRI for evaluating a preclinical C6 GBM rat model. This work began with overcoming the challenges associated with the implementation of the DA3DPR sequence and understanding the limitations of what was achievable given our equipment. This involved tuning and matching the sodium surface coil while loaded with a phantom and examining the performance of the coil over repeated imaging experiments. Ultimately, the protocol was optimized for imaging in clinical imaging mode at 3mm isotropic resolution. The use of a shift reagent and reference vials allowed for repeatable control of the RF transmit gain and correction of the non-uniform surface coil sensitivity profile. This permitted extraction of absolute measurements of the *in vivo* tissue sodium concentration throughout the entire rat head.

Longitudinal animal imaging experiments evaluated changes in TSC over time between a non-treated group (control) and a treatment group which received chemotherapy in the form of TMZ. These experiments showed that TSC increased over time as it was correlated with tumour growth. TSC within the tumour increased with both tumour volume and growth rate. No differences were ultimately found between the non-treated group and the treatment group when examining effects of treatment on TSC. Imaging was also able to clearly differentiate between tumour TSC and TSC in the tumour free contralateral brain region at endpoint. While TSC in the tumours was not significantly different between groups there was a slight difference in doubling time in the treatment group compared to the non-treatment group, with the treatment group having a slightly greater doubling time although this difference was not significant.

In summary, this study demonstrated the feasibility of sodium MRI for pre-clinical research. An imaging pipeline for sodium MRI and image processing was established and longitudinal imaging was evaluated. This study showed that sodium MRI offers complementary information to clinical MR scans typically used for evaluating GBM. Sodium imaging was able to characterize some difference between CE T_1-weighted images and T_2-weighted images and has potential to be sensitive to tumour growth. Overall, there is potential for sodium MRI to be a useful molecular imaging biomarker for cancer in addition to the current techniques for non-invasively monitoring tumours.

4.1.1 Limitations

There were several limitations which affect the conclusions that can be drawn from the results of this study. First it is important to note that there was no longitudinal histology to validate changes observed in the proton or sodium MR. Histology for time matched longitudinal points (at each imaging session) would have provided the gold standard against which, imaging results could be validated. It's important to note that the endpoint histology presented here is most likely obtained when the tumour is the largest on the imaging and therefore the most visible. Being able to more concretely correlate tumour morphology to histology at earlier time points would have strengthened our understanding of the reliability of sodium MR. However, to acquire this data would have required large numbers of animals, been time-consuming, and costly.

The limited sample size (n=7) for this study made it difficult to draw firm conclusions or differentiate if observed trends were significant. This is also significant considering the large biological variation observed from individual animals with regards to tumour progression. Increasing sample size would increase the statistical power for the analyses and allow for concrete conclusions to be drawn regarding trends and patterns observed within and between non-treatment and treatment groups.

The experimental timeline that we chose from a previous imaging study ultimately resulted in difficulty observing treatment effects for this work. A high number of cells (10^6) were initially injected into the animal and allowed to grow over time. This resulted in a more rapid timeline for disease progression as well as more aggressive tumour growth. The treatment regime was unable to successfully combat the tumour burden, and the effects of chemotherapy additionally impacted animal health. Ultimately, we were unable to follow animals' post-treatment to determine if treatment had any long-term effects on TSC. By improving the experimental protocol/timeline and allowing for a slower disease progression it is likely that post-treatment survival time could be increased, and treatment effects might be more clearly observed. The effect of a prolonged timeline has been observed in a slightly different model at higher field strengths. By decreasing the number of cells initially injected and increasing the length of the experiment, they were able to follow animals in the treatment cohort over the course of 45 days [1]. This is much longer even compared to results from a hyperpolarized ^{13}C imaging study which used this same animal model and an expanded treatment regimen where survival was only observed to an average of 18 days [2].

It is also important to recognize the limitations inherent to sodium MRI presented by the hardware and the modality itself. The resolution for the sodium imaging was 3mm isotropic at a field strength of 3T. It should be noted that this is similar to what other researchers have achieved at this field strength for *in vivo* imaging. In the context of a rat brain which is approximately 600mm^3, this leaves an average of 200 pixels for the brain [3]. This resolution limits the comparison we can draw between the anatomical references and the sodium images as smaller areas in the higher resolution T_1-weighted and T_2-weighted proton images will not be quantifiable in the sodium images. Quantification using sodium imaging is additionally limited due to PVE due to the relative pixel to tumour size. Taking into consideration regions of tumour visible on proton scans and not visible on sodium due to voxel size differences, as well as voxels at the boarder of the tumour which capture sodium signal both from tumorous and non-tumorous brain regions. Improvements in sodium MR resolution would reduce the impact of PVE, however this may only be possible with more SNR-efficient sequences or imaging at higher field strengths. It should be noted that increasing SNR at higher field strengths is ultimately limited in terms of applicability as such applications cannot be replicated in humans and TSC in rodent and other mammal tissues is similar to that in humans.

4.1.2 Future work

Future work for this study would include improvements to the pre-clinical model which would allow animals to be evaluated over longer periods of time. This would ultimately allow for the determination of any potential changes to TSC impacted by treatment. Furthermore, the addition of treatment groups in addition to stand-alone chemotherapy could lead to a more clinically relevant study. Current standard of care for GBM includes concurrent chemo-radiotherapy. By including animal groups which receive a combination of chemo-radiotherapy compared to those individual therapies could improve our understanding of how TSC changes in response to different therapies. Further work could include patient derived xenograft (PDX) models for GBM. As the cancer in these models would be derived from patients, they are more likely to recapitulate the biological behaviour of the tumours in humans and are more likely to respond to treatment similar to clinical response [4-6].

The addition of other molecular imaging techniques to our imaging can complement the information we learn from sodium MRI. Modalities such as PET or magnetic resonance spectroscopic imaging (MRSI) of hyperpolarized ^{13}C metabolites can provide additional information specific to the metabolic characteristics of the tumour as well as the environment within and surrounding the tumour [2]. The combination of metabolic information gained from hyperpolarized ^{13}C MRSI within the tumour environment combined with information gained from sodium MRI would provide new insight into understanding the relationship between these techniques as well as gaps between the metabolic characteristics and the morphological characteristics proffered by anatomical T_1-weighted or T_2-weighted imaging.

4.1.3 Significance and impact

It is important to recognize the challenges that GBM poses for disease management. It is difficult to treat, requiring aggressive therapies and current clinical practices have not evolved significantly in over a decade [7]. Improving diagnostic and quantitative techniques provide new avenues for interrogating treatment response and tumour biology. The development of sodium MRI and its improvements has applications for a variety of diseases and conditions [8-10]. Sodium is the second most bio-available nucleus suitable for MR imaging and provides information related to the biochemistry of the cells rather than solely the morphology. By implementing the ability to obtain sodium and proton MR images at 3T we demonstrate the potential this modality has for more applications at clinical field strengths. In conclusion, this thesis provides a baseline for future longitudinal animal studies looking to incorporate sodium MRI into studies of treatment response and evaluating what information can be derived from multi-nuclear imaging at a more clinically relevant field strength.

4.2 References for Chapter 4

1. Schepkin, V.D., et al., *Sodium magnetic resonance imaging of chemotherapeutic response in a rat glioma.* Magnetic resonance in medicine, 2005. **53**(1): p. 85-92.
2. Lim, H., et al., *Monitoring Early Changes in Tumor Metabolism in Response to Therapy Using Hyperpolarized (13)C MRSI in a Preclinical Model of Glioma.* Tomography (Ann Arbor, Mich.), 2020. **6**(3): p. 290-300.
3. Sahin, B., et al., *BRAIN VOLUMES OF THE LAMB, RAT AND BIRD DO NOT SHOW HEMISPHERIC ASYMMETRY: A STEREOLOGICAL STUDY.* 2011, 2011. **20**(1): p. 5.
4. Kijima, N. and Y. Kanemura, *Mouse Models of Glioblastoma*, in *Glioblastoma*, S. De Vleeschouwer, Editor. 2017, Codon Publications Copyright: The Authors.: Brisbane (AU).
5. Joo, K.M., et al., *Patient-specific orthotopic glioblastoma xenograft models recapitulate the histopathology and biology of human glioblastomas in situ.* Cell Rep, 2013. **3**(1): p. 260-73.
6. Patrizii, M., et al., *Utility of Glioblastoma Patient-Derived Orthotopic Xenografts in Drug Discovery and Personalized Therapy.* Front Oncol, 2018. **8**: p. 23.
7. Young, R.M., et al., *Current trends in the surgical management and treatment of adult glioblastoma.* Ann Transl Med, 2015. **3**(9): p. 121.
8. Kopp, C., et al., *23Na magnetic resonance imaging-determined tissue sodium in healthy subjects and hypertensive patients.* Hypertension, 2013. **61**(3): p. 635-40.
9. Huhn, K., et al., *Potential of Sodium MRI as a Biomarker for Neurodegeneration and Neuroinflammation in Multiple Sclerosis.* Frontiers in neurology, 2019. **10**: p. 84-84.
10. Thulborn, K.R., *Quantitative sodium MR imaging: A review of its evolving role in medicine.* NeuroImage, 2018. **168**: p. 250-268.

Appendix

Appendix A. – Animal Research Ethics Approval

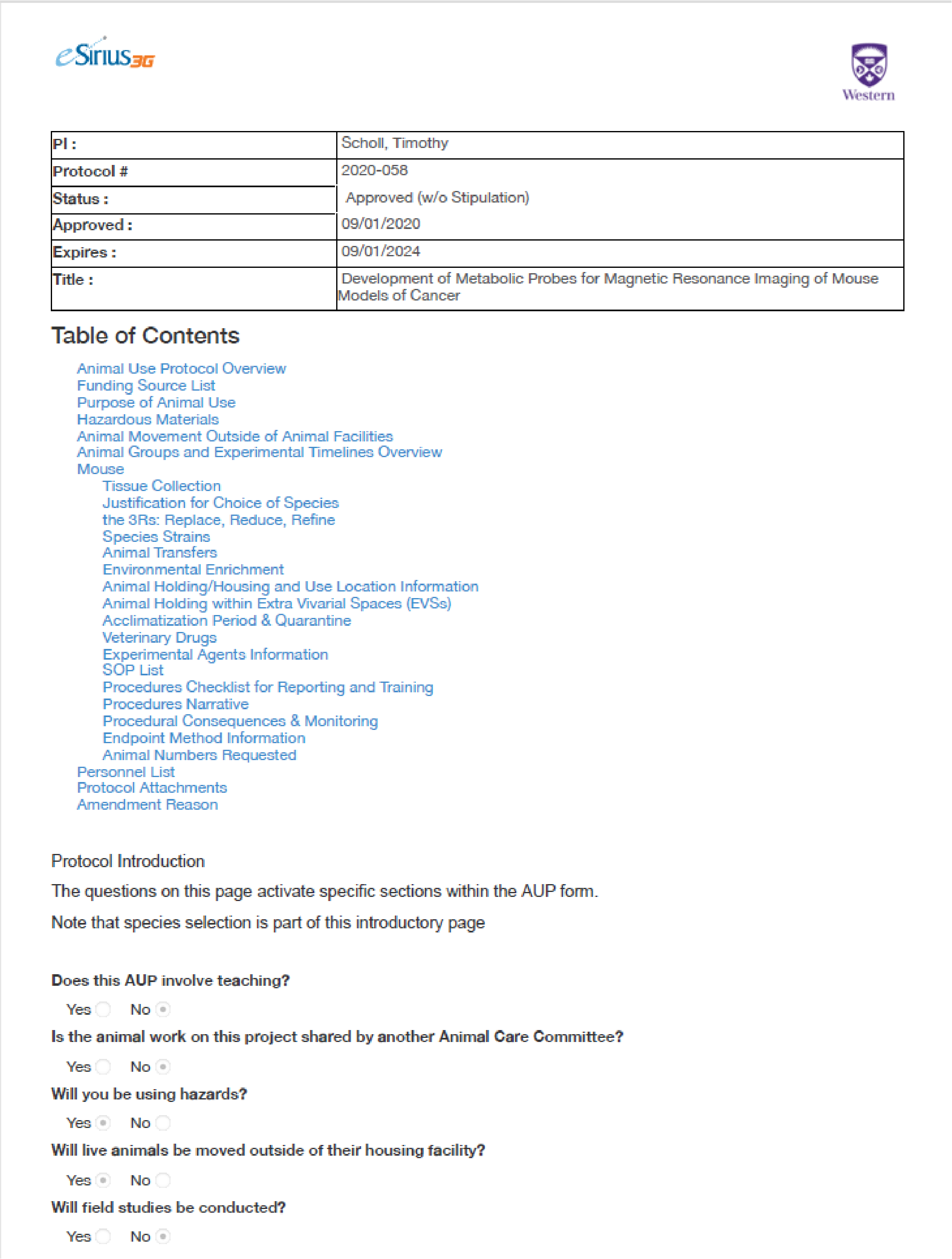

eSirius3G

Western

PI :	Scholl, Timothy
Protocol #	2020-058
Status :	Approved (w/o Stipulation)
Approved :	09/01/2020
Expires :	09/01/2024
Title :	Development of Metabolic Probes for Magnetic Resonance Imaging of Mouse Models of Cancer

Table of Contents

Protocol Introduction

The questions on this page activate specific sections within the AUP form.

Note that species selection is part of this introductory page

Does this AUP involve teaching?

Yes ○ No ●

Is the animal work on this project shared by another Animal Care Committee?

Yes ○ No ●

Will you be using hazards?

Yes ● No ○

Will live animals be moved outside of their housing facility?

Yes ● No ○

Will field studies be conducted?

Yes ○ No ●

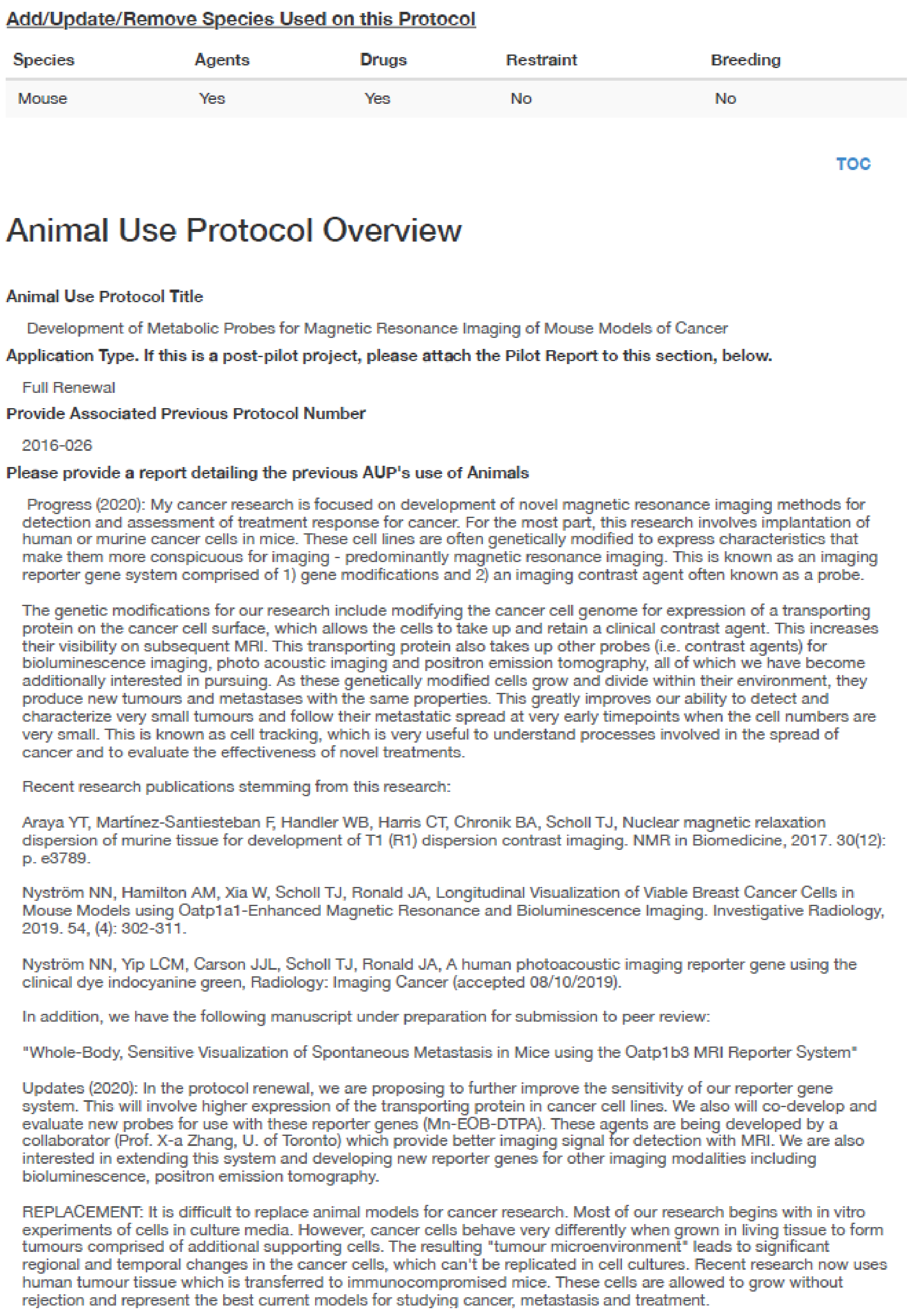

Add/Update/Remove Species Used on this Protocol

Species	Agents	Drugs	Restraint	Breeding
Mouse	Yes	Yes	No	No

TOC

Animal Use Protocol Overview

Animal Use Protocol Title

Development of Metabolic Probes for Magnetic Resonance Imaging of Mouse Models of Cancer

Application Type. If this is a post-pilot project, please attach the Pilot Report to this section, below.

Full Renewal

Provide Associated Previous Protocol Number

2016-026

Please provide a report detailing the previous AUP's use of Animals

Progress (2020): My cancer research is focused on development of novel magnetic resonance imaging methods for detection and assessment of treatment response for cancer. For the most part, this research involves implantation of human or murine cancer cells in mice. These cell lines are often genetically modified to express characteristics that make them more conspicuous for imaging - predominantly magnetic resonance imaging. This is known as an imaging reporter gene system comprised of 1) gene modifications and 2) an imaging contrast agent often known as a probe.

The genetic modifications for our research include modifying the cancer cell genome for expression of a transporting protein on the cancer cell surface, which allows the cells to take up and retain a clinical contrast agent. This increases their visibility on subsequent MRI. This transporting protein also takes up other probes (i.e. contrast agents) for bioluminescence imaging, photo acoustic imaging and positron emission tomography, all of which we have become additionally interested in pursuing. As these genetically modified cells grow and divide within their environment, they produce new tumours and metastases with the same properties. This greatly improves our ability to detect and characterize very small tumours and follow their metastatic spread at very early timepoints when the cell numbers are very small. This is known as cell tracking, which is very useful to understand processes involved in the spread of cancer and to evaluate the effectiveness of novel treatments.

Recent research publications stemming from this research:

Araya YT, Martínez-Santiesteban F, Handler WB, Harris CT, Chronik BA, Scholl TJ, Nuclear magnetic relaxation dispersion of murine tissue for development of T1 (R1) dispersion contrast imaging. NMR in Biomedicine, 2017. 30(12): p. e3789.

Nyström NN, Hamilton AM, Xia W, Scholl TJ, Ronald JA, Longitudinal Visualization of Viable Breast Cancer Cells in Mouse Models using Oatp1a1-Enhanced Magnetic Resonance and Bioluminescence Imaging. Investigative Radiology, 2019. 54, (4): 302-311.

Nyström NN, Yip LCM, Carson JJL, Scholl TJ, Ronald JA, A human photoacoustic imaging reporter gene using the clinical dye indocyanine green, Radiology: Imaging Cancer (accepted 08/10/2019).

In addition, we have the following manuscript under preparation for submission to peer review:

"Whole-Body, Sensitive Visualization of Spontaneous Metastasis in Mice using the Oatp1b3 MRI Reporter System"

Updates (2020): In the protocol renewal, we are proposing to further improve the sensitivity of our reporter gene system. This will involve higher expression of the transporting protein in cancer cell lines. We also will co-develop and evaluate new probes for use with these reporter genes (Mn-EOB-DTPA). These agents are being developed by a collaborator (Prof. X-a Zhang, U. of Toronto) which provide better imaging signal for detection with MRI. We are also interested in extending this system and developing new reporter genes for other imaging modalities including bioluminescence, positron emission tomography.

REPLACEMENT: It is difficult to replace animal models for cancer research. Most of our research begins with in vitro experiments of cells in culture media. However, cancer cells behave very differently when grown in living tissue to form tumours comprised of additional supporting cells. The resulting "tumour microenvironment" leads to significant regional and temporal changes in the cancer cells, which can't be replicated in cell cultures. Recent research now uses human tumour tissue which is transferred to immunocompromised mice. These cells are allowed to grow without rejection and represent the best current models for studying cancer, metastasis and treatment.

REDUCTION: Wherever possible we use cancer cell pellets for our preliminary imaging experiments prior to mouse tumour models to reduce animal use. Because our imaging reporter genes increase the sensitivity for imaging, we can assess tumour growth and metastasis non-invasively in a longitudinal tumour experiment. This means that we cause fewer numbers of animals measuring the tumour growth, metabolism and response to treatment at each experimental timepoint prior to sacrifice and endpoint histology. The resulting experimental data is nearly identical or perhaps even better to experiments using larger animal numbers sacrificed at various experimental timepoints.

REFINEMENT: We will continue our efforts to minimize pain and stress for the animals by using less invasive cell implantation methods (nipple injections versus surgical implantation after incision). Animals will be closely monitored as tumours grow and will be sacrificed if suffering distress as a result of the tumour burden.

2016: We have used magnetic resonance imaging to non-invasively image metabolism and molecular processes in MDA-MB-231 breast tumours implanted into mice (2011 - 2015, AUP #2011-085). We developed two different imaging tools for tumour imaging using murine cancer models: metabolic imaging of hyperpolarized 13C-enriched compounds and fast field-cycling magnetic resonance imaging of targeted paramagnetic compounds.

PROGRESS: For more accurate and precise detection of these cells within animals, more recently (2016 - 2018), we developed a reporter gene technology to non-invasively track viable MDA-MB-231 breast cancer cell distribution via magnetic resonance imaging.

FUTURE: Our next steps (2019 - 2021) focus on improving this reporter gene technology further with a safer and more sensitive manganese-based probe (instead of gadolinium) for standard MRI and fast field-cycling MRI, as well as extending our reporter gene technology to the more accessible platform of dual-energy CT.

PURPOSE: Ultimately, our research is focused on developing translational magnetic resonance imaging tools and knowledge for non-invasive characterization of tumour aggressiveness and for assessment of treatment response.

UPDATES: In this new protocol, we are proposing to apply the imaging tools developed in our previous protocol (2011-085) to an expanded study of new contrast mechanisms. These include a new Mn-based contrast agent for standard MRI and our fast field-cycling MRI platform, and extending our gadolinium-based contrast mechanisms to include dual-energy CT detection. Imaging data will be compared with histopathology to establish whether our MRI/CT methods can accurately measure differences in the detection of breast cancer cells using either safer and more sensitive (Mn/MRI) or more accessible (Gd dual energy CT) modalities.

As a result, this new protocol is seeking a larger cohort of mice (total of 60 mice) for imaging of an expanded group of different breast cancer cell lines.

REPLACEMENT: Eventual clinical translation of our tumour imaging methods requires in vivo research using realistic tumour models exhibiting tumour progression, which is similar to that experienced in humans. Murine models of cancer are well established and an accepted stepping stone in the path to clinical translation. We expect that our methods will eventually be useful for human imaging of cancer.

REDUCTION: We have used imaging phantoms (paramagnetic liquids with known MRI properties) or ex vivo tissue, whenever possible to develop the hardware for magnetic field cycling MRI. We recover our animals from anesthesia after our imaging experiments for repeated imaging. Cohorts of tumour-bearing animals are imaged in longitudinal experiments until established experimental endpoints using the minimum numbers possible to achieve experimental outcomes.

REFINEMENT: We will continue our efforts to minimize pain and stress for the animals by using less invasive cell implantation methods (nipple injections versus surgical implantation after incision). Animals will be closely monitored as tumours grow and will be sacrificed if suffering distress as a result of the tumour burden.

Using non-scientific language, please describe the project's purpose, expected benefit, and a brief summary of your work with the animal model(s).

This animal protocol involves the development and evaluation of a multimodality imaging report gene system for imaging and tracking cells. This imaging reporter gene system is a combination of cells whose genome is modified through genome editing to add a protein to their surface and a contrast agent known as a probe, that is specifically transported by that protein into the cell where its retention increase the visibility of a group of those cells during imaging. In this protocol, gene-edited cells are injected into animals and imaged with magnetic resonance imaging (MRI), bioluminescence imaging (BLI) or photoacoustic imaging (PAI) after injection of the appropriate probe (Gd-EOB-DTPA, D-Luciferin or Indocyanine Green respectively). This increases the sensitivity of the imaging so that a fewer number of cells can be detected. This is useful for cancer research, where smaller tumours and their metastases often cannot be found by imaging until they are much larger. Only cells, which have been genetically modified and are alive will be enhanced by administration of the probe.

One important future application of this technology is to monitor chimeric antigen receptor T cell (i.e. CAR-T cell) immunotherapy used for treatment of cancer. Although novel immunotherapies such as CAR-T cells are making the news as they are being trialed in patients, the technology to track these cells in order to monitor patient-specific response and to understand treatment failure and potentially life-threatening toxicities has lagged these therapies. Effective monitoring requires sensitive non-invasive imaging to determine where the cells migrate, their survival and treatment effects. Existing tools for cell tracking have been limited mostly to animal models due to safety considerations with human use and their limited sensitivity or lack of utility for long-term tracking. This preclinical research seeks to develop sensitive cell tracking technology compatible with eventual human research. For example, the transporting protein that we are using is human in origin (normally found in liver cells) and the probe for MRI is a clinical contrast agent used for finding liver tumours.

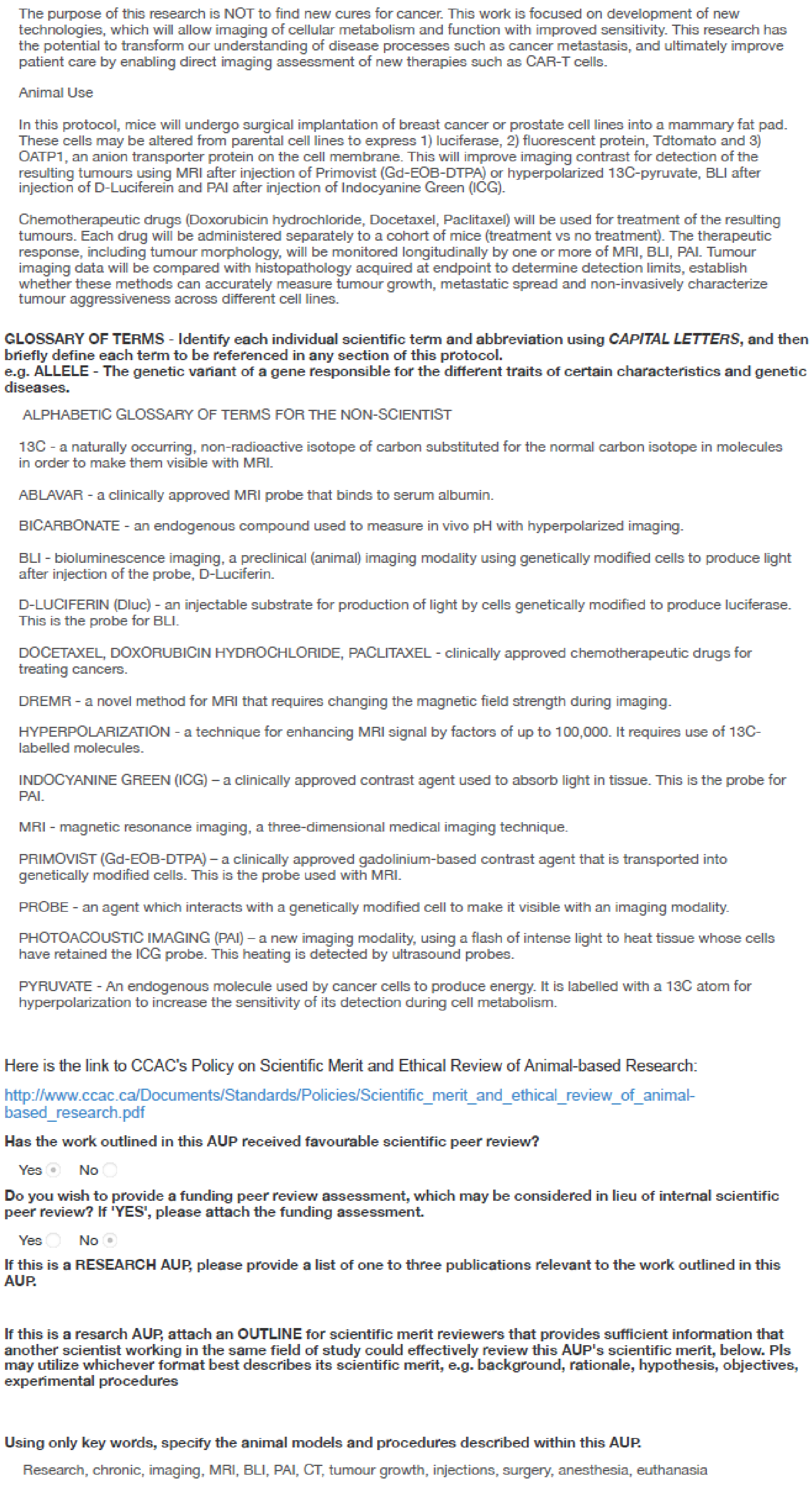

The purpose of this research is NOT to find new cures for cancer. This work is focused on development of new technologies, which will allow imaging of cellular metabolism and function with improved sensitivity. This research has the potential to transform our understanding of disease processes such as cancer metastasis, and ultimately improve patient care by enabling direct imaging assessment of new therapies such as CAR-T cells.

Animal Use

In this protocol, mice will undergo surgical implantation of breast cancer or prostate cell lines into a mammary fat pad. These cells may be altered from parental cell lines to express 1) luciferase, 2) fluorescent protein, Tdtomato and 3) OATP1, an anion transporter protein on the cell membrane. This will improve imaging contrast for detection of the resulting tumours using MRI after injection of Primovist (Gd-EOB-DTPA) or hyperpolarized 13C-pyruvate, BLI after injection of D-Luciferein and PAI after injection of Indocyanine Green (ICG).

Chemotherapeutic drugs (Doxorubicin hydrochloride, Docetaxel, Paclitaxel) will be used for treatment of the resulting tumours. Each drug will be administered separately to a cohort of mice (treatment vs no treatment). The therapeutic response, including tumour morphology, will be monitored longitudinally by one or more of MRI, BLI, PAI. Tumour imaging data will be compared with histopathology acquired at endpoint to determine detection limits, establish whether these methods can accurately measure tumour growth, metastatic spread and non-invasively characterize tumour aggressiveness across different cell lines.

GLOSSARY OF TERMS - Identify each individual scientific term and abbreviation using *CAPITAL LETTERS*, and then briefly define each term to be referenced in any section of this protocol.
e.g. ALLELE - The genetic variant of a gene responsible for the different traits of certain characteristics and genetic diseases.

ALPHABETIC GLOSSARY OF TERMS FOR THE NON-SCIENTIST

13C - a naturally occurring, non-radioactive isotope of carbon substituted for the normal carbon isotope in molecules in order to make them visible with MRI.

ABLAVAR - a clinically approved MRI probe that binds to serum albumin.

BICARBONATE - an endogenous compound used to measure in vivo pH with hyperpolarized imaging.

BLI - bioluminescence imaging, a preclinical (animal) imaging modality using genetically modified cells to produce light after injection of the probe, D-Luciferin.

D-LUCIFERIN (Dluc) - an injectable substrate for production of light by cells genetically modified to produce luciferase. This is the probe for BLI.

DOCETAXEL, DOXORUBICIN HYDROCHLORIDE, PACLITAXEL - clinically approved chemotherapeutic drugs for treating cancers.

DREMR - a novel method for MRI that requires changing the magnetic field strength during imaging.

HYPERPOLARIZATION - a technique for enhancing MRI signal by factors of up to 100,000. It requires use of 13C-labelled molecules.

INDOCYANINE GREEN (ICG) – a clinically approved contrast agent used to absorb light in tissue. This is the probe for PAI.

MRI - magnetic resonance imaging, a three-dimensional medical imaging technique.

PRIMOVIST (Gd-EOB-DTPA) – a clinically approved gadolinium-based contrast agent that is transported into genetically modified cells. This is the probe used with MRI.

PROBE - an agent which interacts with a genetically modified cell to make it visible with an imaging modality.

PHOTOACOUSTIC IMAGING (PAI) – a new imaging modality, using a flash of intense light to heat tissue whose cells have retained the ICG probe. This heating is detected by ultrasound probes.

PYRUVATE - An endogenous molecule used by cancer cells to produce energy. It is labelled with a 13C atom for hyperpolarization to increase the sensitivity of its detection during cell metabolism.

Here is the link to CCAC's Policy on Scientific Merit and Ethical Review of Animal-based Research:

http://www.ccac.ca/Documents/Standards/Policies/Scientific_merit_and_ethical_review_of_animal-based_research.pdf

Has the work outlined in this AUP received favourable scientific peer review?

Yes ● No ○

Do you wish to provide a funding peer review assessment, which may be considered in lieu of internal scientific peer review? If 'YES', please attach the funding assessment.

Yes ○ No ●

If this is a RESEARCH AUP, please provide a list of one to three publications relevant to the work outlined in this AUP.

If this is a resarch AUP, attach an OUTLINE for scientific merit reviewers that provides sufficient information that another scientist working in the same field of study could effectively review this AUP's scientific merit, below. PIs may utilize whichever format best describes its scientific merit, e.g. background, rationale, hypothesis, objectives, experimental procedures

Using only key words, specify the animal models and procedures described within this AUP.

Research, chronic, imaging, MRI, BLI, PAI, CT, tumour growth, injections, surgery, anesthesia, euthanasia

Appendix B. – Sodium surface coil intensity correction MATLAB script

Read Sensitivity Map

```
load nMap.mat
load mP.mat
```

Read Test Image

```
I = double(niftiread('RatSodium.nii.gz'));           % Phantom
IM=double(niftiread('RatSodium.mask.nii.gz'));   % Mask

%I = imgaussfilt(I, 20);

% Erode the mask (OPTIONAL)
se1=strel('disk',10);
se2=strel('disk',25);

%se=strel('sphere',2);
IM=imerode(IM,se1); % erode mask

% The final Mask is the AND function of the image mask and the sensitivity mask
Mask=IM.*mP;
MI=I.*Mask;
```

Display Test Image

```
figure(10)  % original image
montage(reshape(I,512,512,1,27))
caxis('auto')
colorbar

% Display final Mask
figure(11)  % image of mask
montage(reshape(Mask,512,512,1,27))
caxis('auto')
colorbar

% Display masked image
figure(12)  % eroded and multipled mask
montage(reshape(MI,512,512,1,27))
caxis('auto')
colorbar

% Display Sensitivity Map
figure(13)  % sensitivity mask
montage(reshape(nMap,512,512,1,27))
```

```
caxis('auto')
colorbar
```

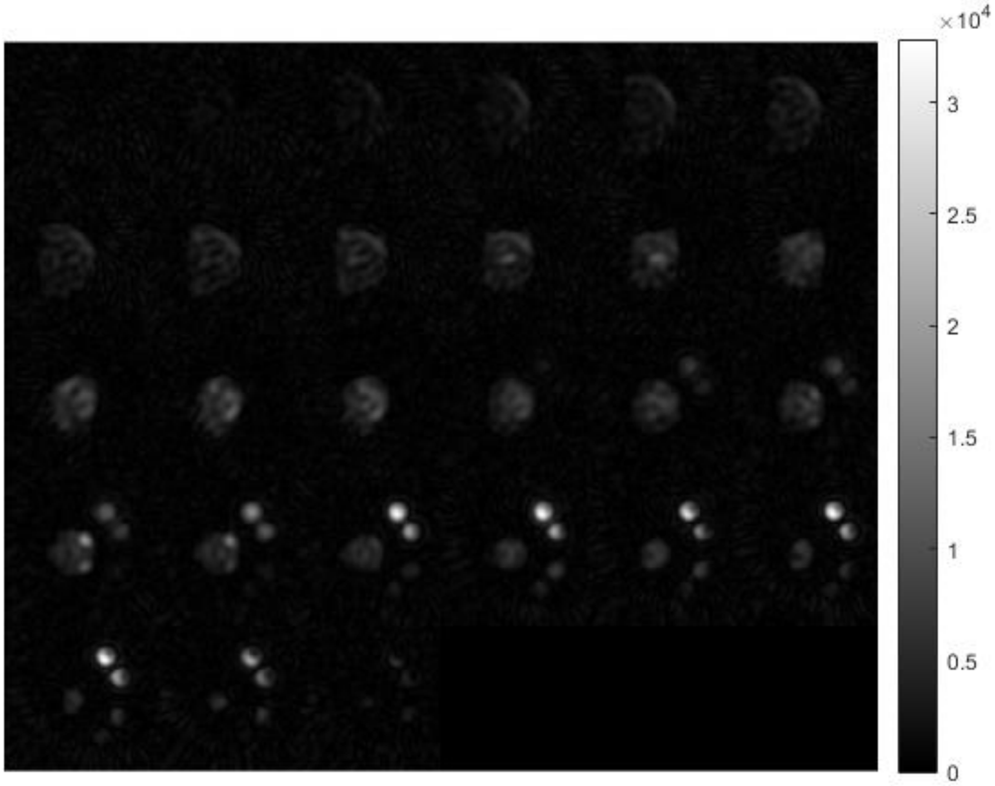

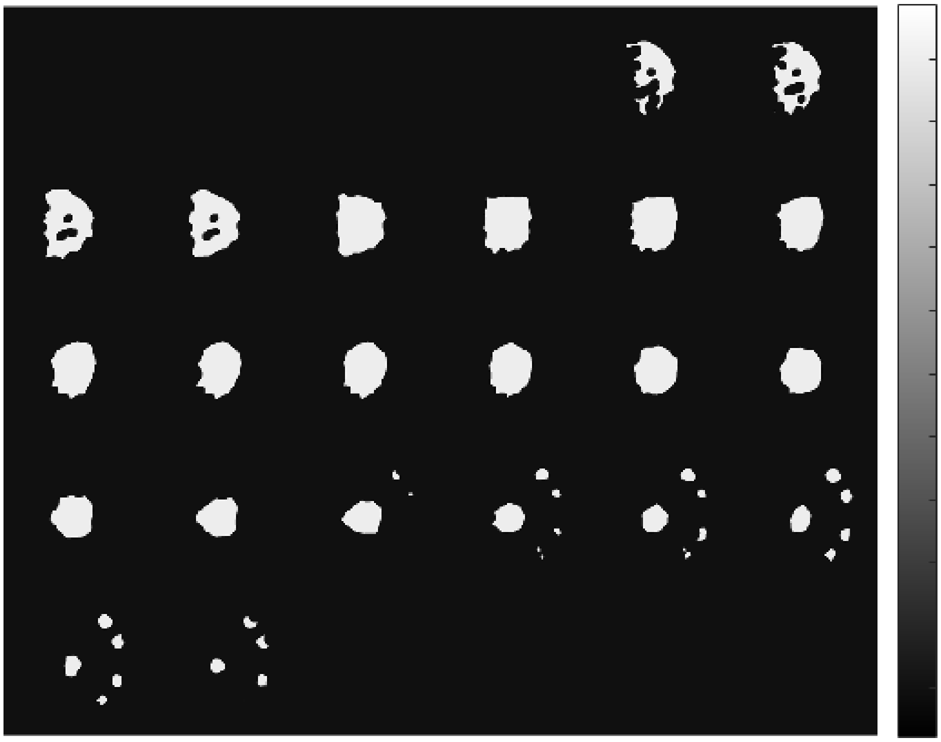
1
0.9
0.8
0.7
0.6
0.5
0.4
0.3
0.2
0.1
0

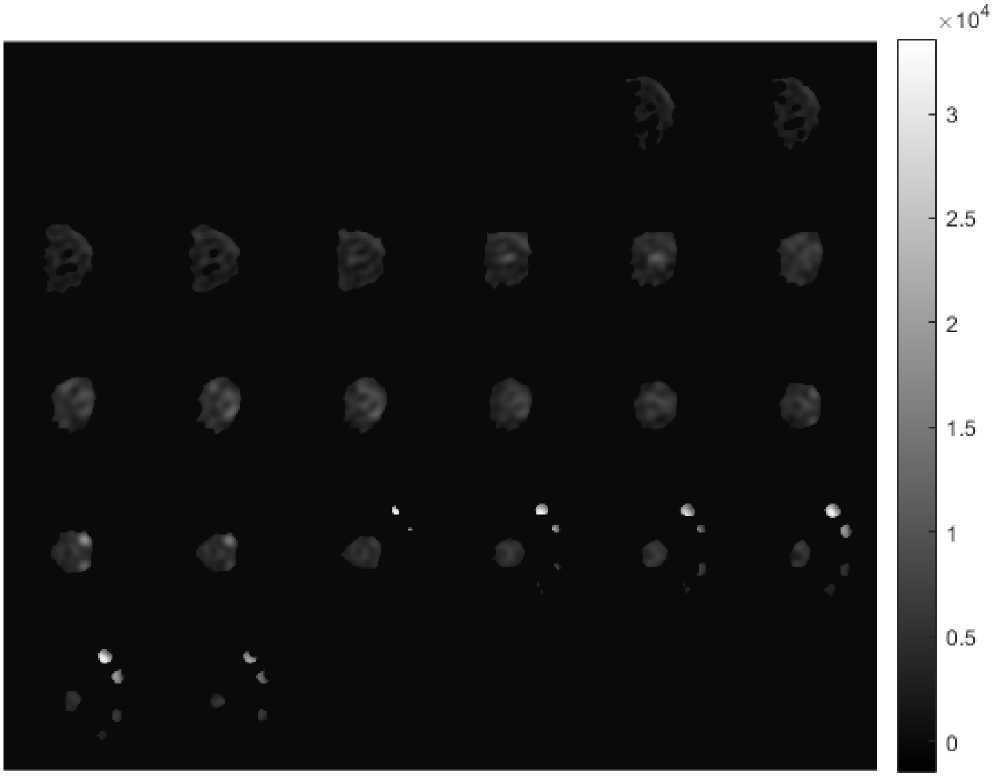
×10^4
3
2.5
2
1.5
1
0.5
0

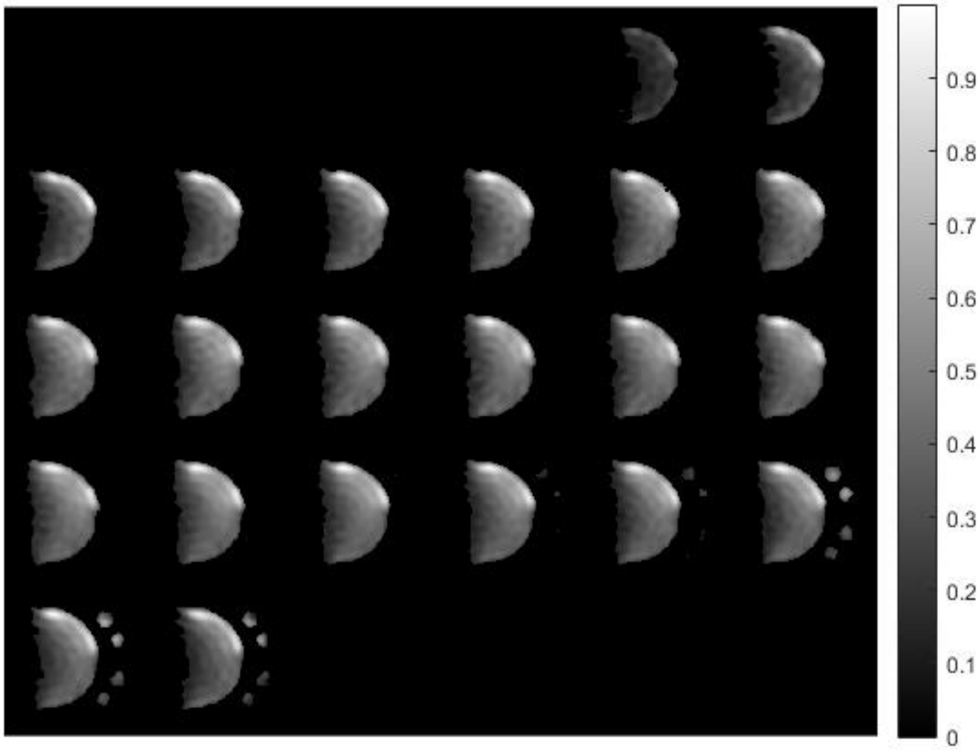

Obtain the noise level

```
%restrict to the first 18 slices
mask2 = Mask(:,:,1:18); % addressed the PSF by grabbing everything from slices that don't
contain vials
I2 = I(:,:,1:18);

Inv_Mask=1-mask2; % 0's where the object is, -1 everywhere else

Inv_Mask=imerode(Inv_Mask,se2); % erode into the noise space (big)

indx=find(Inv_Mask); % returns all non-zero indicies

noise_level=mean(I2(indx)); % uses those indices to find the mean noise from the original
image

std_noise=std(I2(indx)); % standard deviation of all the noise things
```

Obtain Image with Sensitivity Compensation

```
%subtract offset from image
MI = MI - noise_level;
MI(MI<=0) = 0;

ISC=MI./nMap; %sensitivity compensation
ISC(isinf(ISC))=0;
ISC(ISC==0)=NaN;

figure(14)
montage(reshape(ISC,512,512,1,27))
caxis('auto')
colorbar
```

Obtain Regions

```
CC=bwconncomp(Mask);
% get the info from the image using the mask connected pixels
new_stats=regionprops3(CC,ISC,'Volume','VoxelIdxList','MaxIntensity','MeanIntensity','Min
Intensity','VoxelValues','Centroid','WeightedCentroid');
```

```
figure(15)
colormap(gray)
imagesc(max(ISC,[],3))
hold on
for i=1:height(new_stats)
    text(new_stats.Centroid(i,1),new_stats.Centroid(i,2),num2str(i),'Color','y')
end
title('Regions Identification')
```

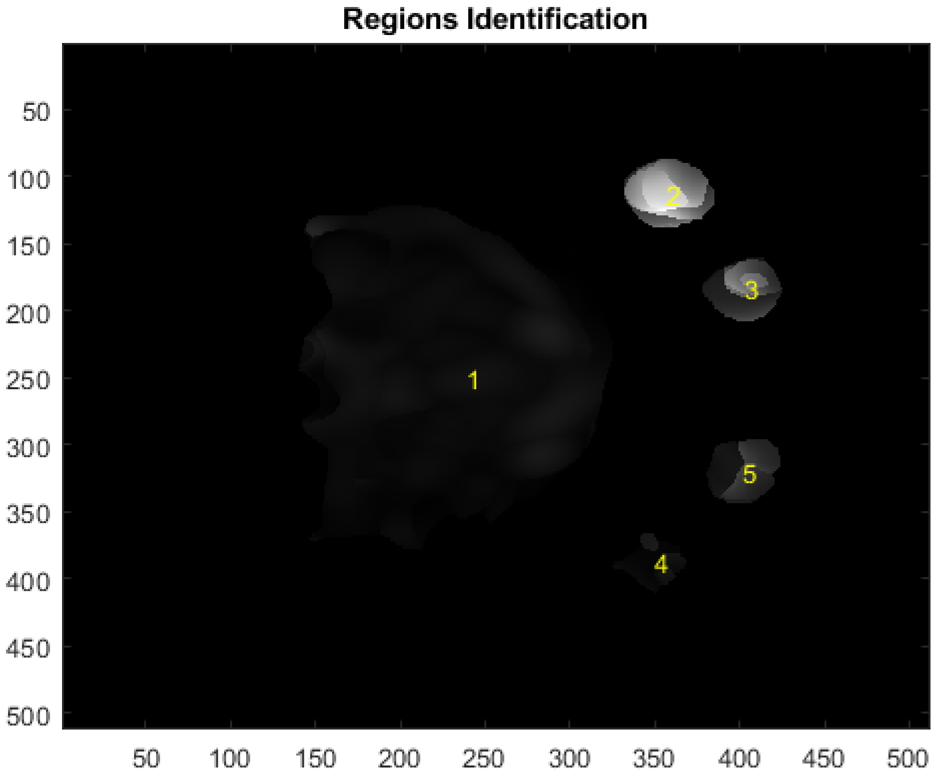

Calibrate image to known concentrations

```
new_stats=regionprops3(CC,ISC,'Volume','VoxelIdxList','MaxIntensity','MeanIntensity','MinIntensity','VoxelValues','Centroid','WeightedCentroid');
C=[30,50,70,100];

% Localize the vials
indx_c=find_conc;

% Obtain Mean and Standard Deviations for each object
stdev(1)=std(new_stats.VoxelValues{indx_c(1)});
stdev(2)=std(new_stats.VoxelValues{indx_c(2)});
stdev(3)=std(new_stats.VoxelValues{indx_c(3)});
stdev(4)=std(new_stats.VoxelValues{indx_c(4)});
%stdev(5)=std_noise;

x(1)=new_stats.MeanIntensity(indx_c(1));
```

```
x(2)=new_stats.MeanIntensity(indx_c(2));
x(3)=new_stats.MeanIntensity(indx_c(3));
x(4)=new_stats.MeanIntensity(indx_c(4));
%x(5)=noise_level;

% Do linear fitting to obtain curve Signal Intensity vs. Concentration
mdl=fitlm(C(2:end),x(2:end));
% Slope
m=mdl.Coefficients.Estimate(2);
% Zero cross
b=mdl.Coefficients.Estimate(1);

% Obtain equation to get curve Concentration vs. Signal Intensity
% Slope
m2=1/m;
% Zero cross
b2=-b/m;

values = linspace(0,100);

% Display linear fitting
figure(16)
errorbar(C,x,stdev,'*k')
hold on
plot(values,m.*values+b,'-b')
hold off
```

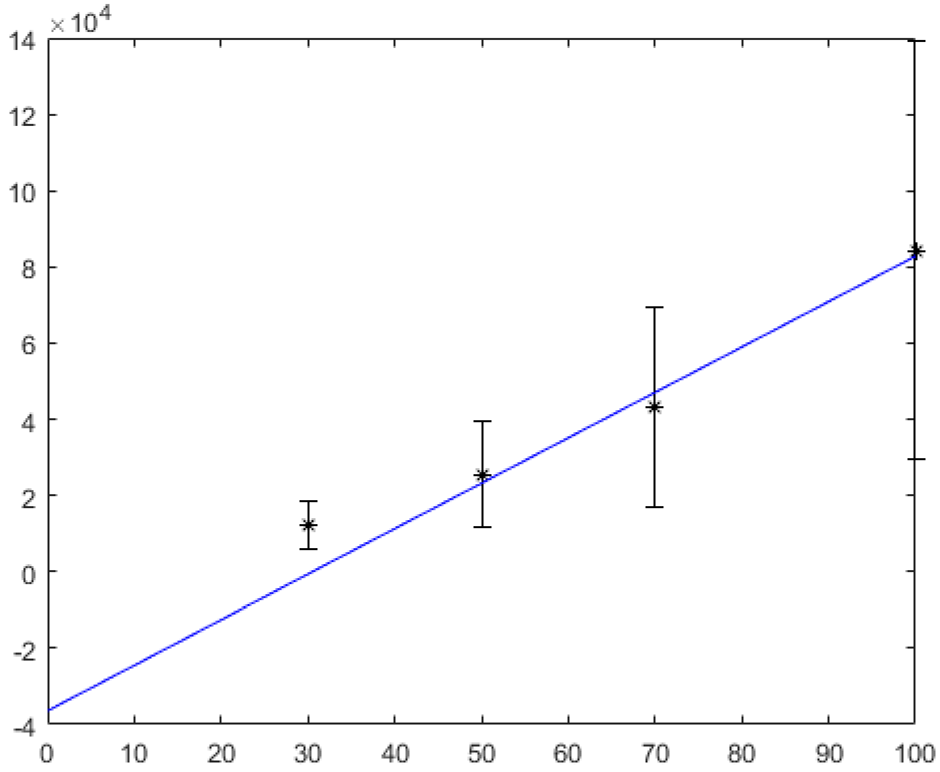

Obtain Concentration Map

```
C_Image=Mask.*(m2.*ISC+b2);
C_Image(C_Image<=0)=0;
C_Image(isnan(C_Image)) = 0;

figure(17)
montage(reshape(C_Image,512,512,1,27))
caxis('auto')
colorbar
```

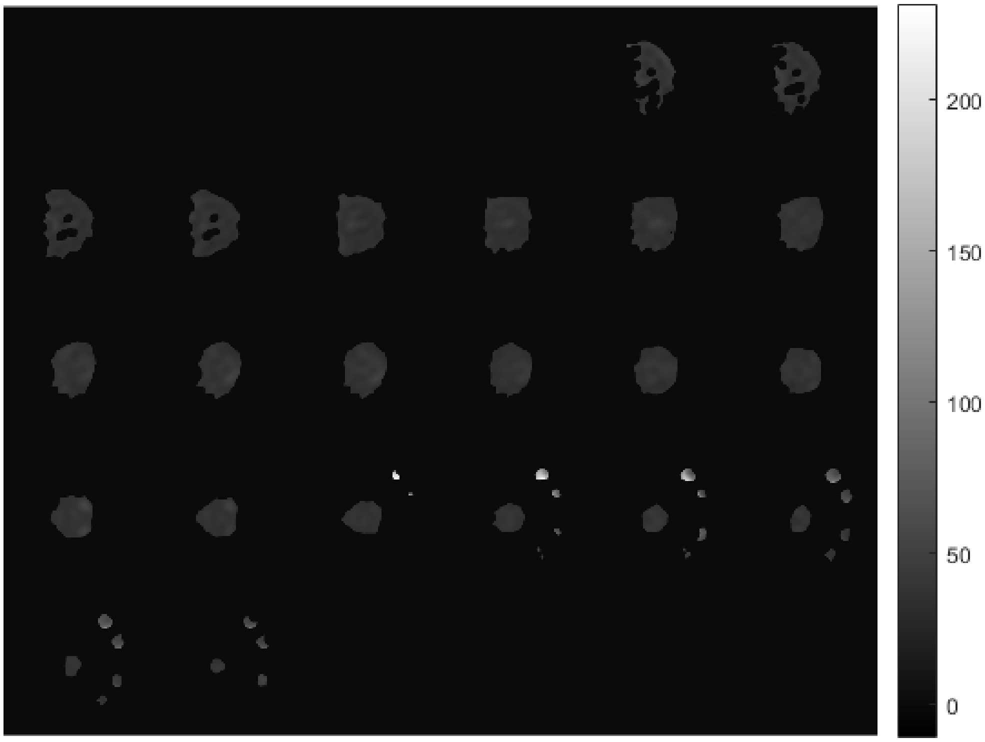

Obtain Mean and Standard Deviation of Concentration Map

```
final_stats=regionprops3(CC,C_Image,'Volume','VoxelIdxList','MaxIntensity','MeanIntensity
','MinIntensity','VoxelValues','Centroid','WeightedCentroid');

figure(18)
imagesc(max(C_Image,[],3))
for i=1:height(final_stats)
    stdev_c(i)=std(final_stats.VoxelValues{i});
```

```
text(final_stats.Centroid(i,1),final_stats.Centroid(i,2),[num2str(final_stats.MeanIntensi
ty(i),4),'+/-',num2str(stdev_c(i),3)],'Color','w')
end
hold on
axis square
title('Regions Identification')
```

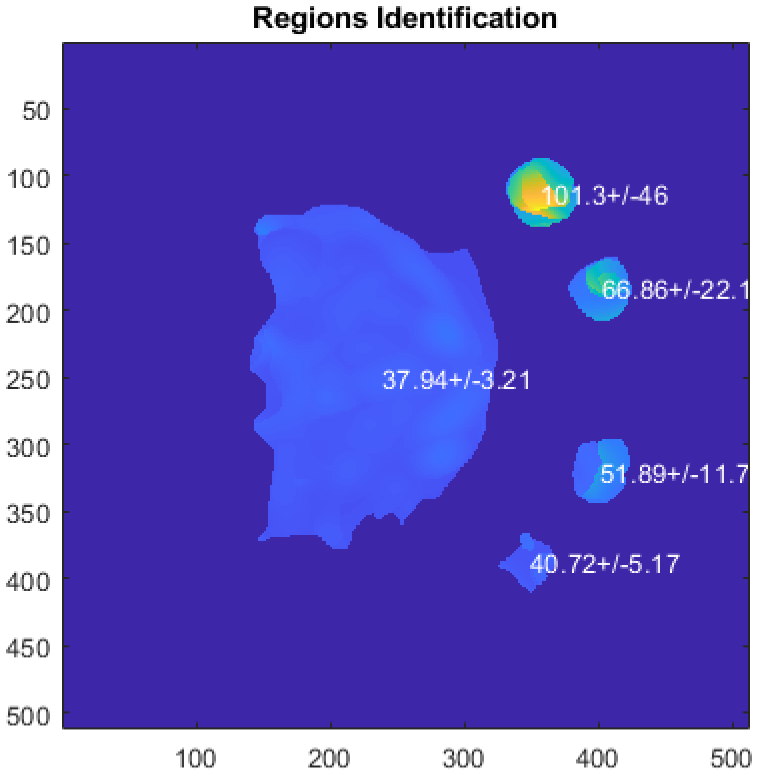

Validate fit from concentration map

Localize the vials

```
indx_c=find_conc;

% Obtain Mean and Standard Deviations for each object
stdev(1)=std(final_stats.VoxelValues{indx_c(1)});
stdev(2)=std(final_stats.VoxelValues{indx_c(2)});
stdev(3)=std(final_stats.VoxelValues{indx_c(3)});
stdev(4)=std(final_stats.VoxelValues{indx_c(4)});
%stdev(5)=std_noise;

x(1)=final_stats.MeanIntensity(indx_c(1));
x(2)=final_stats.MeanIntensity(indx_c(2));
x(3)=final_stats.MeanIntensity(indx_c(3));
x(4)=final_stats.MeanIntensity(indx_c(4));
%x(5)=noise_level;
```

```
% Do linear fitting to oibtain curve Signal Intensity vs. Concentration
mdl2=fitlm(C,x);
% Slope
m3=mdl2.Coefficients.Estimate(2);
% Zero cross
b3=mdl2.Coefficients.Estimate(1);

values = linspace(0,100);

% Display linear fitting
figure(19)
errorbar(C,x,stdev,'*k')
hold on
plot(values,m3.*values+b3,'-b')
hold off
```

Function needed to match reference vials to correct concentration

```
function indx=find_conc;
figure(15) % Just to bring to the front the Region I.D. figure

d = dialog('Position',[300 300 250 150],'Name','Select One');
txt = uicontrol('Parent',d,'Style','text','Position',[20 110 210 40],...
    'String','Select the correct index for each vial with the given concentrations');
txt.FontSize=12;

c1_txt=uicontrol('Parent',d,'Style','text','Position',[70 90 50 20],...
    'String','30 mM','HorizontalAlignment','right');
c1_edit=uicontrol('Parent',d,'Style','edit','Position',[120 95 50
15],'Callback',@edit_c1);

c2_txt=uicontrol('Parent',d,'Style','text','Position',[70 75 50 20],...
    'String','50 mM','HorizontalAlignment','right');
c2_edit=uicontrol('Parent',d,'Style','edit','Position',[120 80 50
15],'Callback',@edit_c2);

c3_txt=uicontrol('Parent',d,'Style','text','Position',[70 60 50 20],...
    'String','70 mM','HorizontalAlignment','right');
c3_edit=uicontrol('Parent',d,'Style','edit','Position',[120 65 50
15],'Callback',@edit_c3);

c4_txt=uicontrol('Parent',d,'Style','text','Position',[70 45 50 20],...
    'String','100 mM','HorizontalAlignment','right');
c4_edit=uicontrol('Parent',d,'Style','edit','Position',[120 50 50
15],'Callback',@edit_c4);

btn = uicontrol('Parent',d,...
           'Position',[89 15 70 25],...
           'String','Close',...
           'Callback','delete(gcf)');

indx=[];
```

```
    function edit_c1(c1_edit,event)
        indx(1)=str2num(c1_edit.String);
    end

    function edit_c2(c2_edit,event)
        indx(2)=str2num(c2_edit.String);
    end

    function edit_c3(c3_edit,event)
        indx(3)=str2num(c3_edit.String);
    end

    function edit_c4(c4_edit,event)
        indx(4)=str2num(c4_edit.String);
    end

% Wait for d to close before running to completion
uiwait(d);

end
```

Published with MATLAB® R2019b

Curriculum Vitae

Education

2018-*present* Master of Science in Medical Biophysics
Department of Medical Biophysics
University of Western Ontario, London, Canada
Supervisor: Dr. Timothy J. Scholl

2014-2018 Bachelors of Medical Sciences
Honors Specialization in Medical Biophysics (Medical Sciences Concentration)
with distinction
Department of Medical Biophysics
University of Western Ontario, London Canada
Thesis:" Validation of hemodynamic parameters of a dynamic neonatal left ventricle phantom"
Supervisor: Dr. James Lacefield

Positions Held

2018-*present* Graduate Research Student • Robarts Research Institute, London, Ontario
Department of Medical Biophysics
University of Western Ontario
Supervisor: Dr. Timothy J. Scholl

2018 Undergraduate Research Student • Robarts Research Institute
Department of Medical Biophysics
University of Western Ontario
Supervisor: Dr. James Lacefield

2017 Undergraduate Research Student • Schulich School of Medicine and Dentistry
Department of Medical Biophysics
University of Western Ontario
Supervisor: Dr. Dwayne Jackson

2016 Undergraduate Research Assistant • Robarts Research Institute
Department of Medical Biophysics
University of Western Ontario
Supervisor: Dr. Ali Khan

Academic Responsibilities

2019 Teaching Assistant (TA)
Department of Medical Biophysics
Medical Biophysics 3501 - Biophysics of Transport Systems

2019 Teaching Assistant (TA)
Department of Medical Biophysics
Medical Biophysics 3507 - Biophysics of Oxygen Transport

Honors and Awards

2020	Poster Presentations Honorable Mentions Imaging Network of Ontario 2020 (IMNO)
2019-2020	Graduate Scholarship - Masters (CGS-M) Natural Science and Engineering Research Council of Canada (NSERC) *Awarded to high-calibre students engaged in a research-based masters focused on the natural sciences or engineering (National – $17500)*
2019-2020	Ontario Graduate Scholarship (OGS) Ontario Graduate Scholarship Program *A merit-based scholarship (based on academic standing) that encourages excellence in graduate studies and is available to students in all disciplines of academic study (Provincial - $15000)* (*Declined)*
2019-2020	Western Graduate Research Scholarship University of Western Ontario *Awarded to full time graduate students for stipend support with a maintained average of 80% or more (Institutional – $5000)*
2018-2019	Western Graduate Research Scholarship University of Western Ontario *Awarded to a full-time graduate student for stipend support with a maintained average of 80% or more (Institutional – $5000)*
2014-2018	Western Continuing Admissions Scholarship University of Western Ontario *Awarded to incoming students with entering averages of 95% or higher (Institutional – $10000)*

Committees and Professional Activities

2019-2020	Robarts Association of Trainees University of Western Ontario *Executive Committee Member*
2019-2020	Medical Biophysics Undergraduate Research Day University of Western Ontario *Organizing Committee Member*
2019-2020	Let’s Talk Cancer University of Western Ontario *Workshop Committee Member*
2016-2017	Global Brainhack Western University of Western Ontario *Organizing Committee Member*

Conference Publications

1. N. Boone, O. Ginty, **X.Y. Wang**, J. Moore, Terry M. Peters, J.C. Lacefield, T. Poepping, D.
Bainbridge. A dynamic neonatal heart phantom for new ”ultrafast” echocardiograpy evaluation. *SPIE Medical Imaging 2018*

Conference Poster Publications

1. **X.Y. Wang**, A. Akbari, F.M. Martinez-Santiesteban, T.J. Scholl. Development of sodium MRI for small animal imaging at 3 Tesla. *The Future of Molecular MR: A Cellular and Molecular Imaging Workshop 2019*
2. **X.Y. Wang**, A. Akbari, F.M. Martinez-Santiesteban, T.J. Scholl. Development of sodium MRI for small animal imaging at 3 Tesla. *Great Lakes Advanced Molecular Imaging Course 2019*
3. **X.Y. Wang**, A. Akbari, F.M. Martinez-Santiesteban, T.J. Scholl. Development of high-resolution sodium RI for rat glioblastoma at 3 Tesla. *Robarts Research Retreat 2019*
4. **X.Y. Wang**, A. Akbari, F.M. Martinez-Santiesteban, T.J. Scholl. Development of high-resolution sodium RI for rat glioblastoma at 3 Tesla. *Oncology Research and Education Day 2019*
5. **X.Y. Wang**, A. Akbari, F.M. Martinez-Santiesteban, T.J. Scholl. Development of high-resolution sodium RI for rat glioblastoma at 3 Tesla. *London Health Research Day 2019*
6. **X.Y. Wang**, A. Akbari, F.M. Martinez-Santiesteban, T.J. Scholl. Implementation of density adapted 3-dimensional projection reconstruction MRI sequence for small animal sodium imaging at 3 Tesla. *Imaging Network of Ontario 2020*
7. **X.Y. Wang**, A. Akbari, F.M. Martinez-Santiesteban, T.J. Scholl. Implementation of density adapted 3-dimensional projection reconstruction MRI sequence for small animal sodium imaging at 3 Tesla. *World Molecular Imaging Congress 2020*